SUPPORTING INFORMATION

Nitrito-*κ*N ligand in pentacyanidocobaltate(III) linkers as a polarity inducer in heterometallic frameworks incorporating lanthanide(III) molecular nanomagnets

Hubert Dzielak,[a] Pawel J. Bonarek,[ab] Jakub J. Zakrzewski,[ac] Shin-ichi Ohkoshi,[c] and Szymon Chorazy*[a]

[a]Faculty of Chemistry, Jagiellonian University, Gronostajowa 2, 30-387 Kraków, Poland. [b]Doctoral School of Exact and Natural Sciences, Jagiellonian University, Lojasiewicza 11, 30-348 Krakow, Poland. [c]Department of Chemistry, School of Science, The University of Tokyo, 7-3-1 Hongo, Bunkyo-ku, Tokyo 113-0033, Japan.

Corresponding author's e-mail: simon.chorazy@uj.edu.pl

Experimental section. S4

The asymmetric units of the crystal structures of **$LaCoNO_2$**, **$CeCoNO_2$**, **$PrCoNO_2$**, and **$SmCoNO_2$**. (Fig. S1) S7

Crystal data and structure refinement parameters for **$LaCoNO_2$**, **$CeCoNO_2$**, and **$PrCoNO_2$**. (Table S1) S8

Crystal data and structure refinement parameters for **$NdCoNO_2$** and **$SmCoNO_2$**. (Table S2) S9

Selected metric parameters for **$LaCoNO_2$**, **$CeCoNO_2$**, **$PrCoNO_2$**, **$NdCoNO_2$**, and **$SmCoNO_2$**, including the selected bond lengths and angles of lanthanide complexes, as well as the distances between the indicated atoms or moieties representing the main detected supramolecular interactions, i.e., hydrogen bonds and π-π stacking. (Table S3) S10

Results of Continuous Shape Measures (CShM) analysis for six-coordinated Co(III) complexes in the **$LnCoNO_2$** series. (Table S4) S11

Results of Continuous Shape Measures (CShM) for nine-coordinated lanthanide(III) complexes in the **$LnCoNO_2$** series. (Table S5) S11

Powder X-ray diffraction (P-XRD) patterns of the obtained compounds. (Fig. S2) S12

Infrared (IR) absorption spectra of **$LaCoNO_2$**, **$CeCoNO_2$**, **$PrCoNO_2$**, **$NdCoNO_2$**, ***d*-$NdCoNO_2$**, and **$SmCoNO_2$**. (Fig. S3) S13

Solid-state UV-vis absorption spectra for the powder samples of **$LaCoNO_2$**, **$CeCoNO_2$**, **$PrCoNO_2$**, **$NdCoNO_2$**, and **$SmCoNO_2$**. (Fig. S4) S14

Thermogravimetric (TG) curves of the powder samples of **$LaCoNO_2$**, **$CeCoNO_2$**, **$PrCoNO_2$**, **$NdCoNO_2$**, and **$SmCoNO_2$**. (Fig. S5) S15

Representative views of the crystal structure of the reference compound of **LaFeCN**. (Fig. S6) S16

Crystal data and structure refinement parameters for the crystal structure of the reference compound of **LaFeCN**. (Table S6) S17

Comparison of the calculated powder X-ray diffraction (P-XRD) patterns of **$LaCoNO_2$** and **LaFeCN**, as well as the experimental P-XRD pattern for the powder sample of **LaCoCN**. (Fig. S7) S18

Results of the fitting of the SHG intensity dependence on laser power to a quadratic function for each compound from the **$LnCoNO_2$** series and for the KDP reference. (Table S7) S18

Room-temperature solid-state emission (right side) and excitation (left side) spectra of **$NdCoNO_2$** and its deuterated sample of ***d*-$NdCoNO_2$**. (Fig. S8) S19

Wavelength dependences of the ratio between the emission intensities under the 582 excitation for ***d*-$NdCoNO_2$** and **$NdCoNO_2$** at room temperature and at the liquid nitrogen temperature. (Fig. S9) S20

Sample masses used for the SQUID magnetometry measurements and the diamagnetic corrections employed in the analysis of the gathered raw magnetic data for **$NdCoNO_2$**, **Nd@$LaCoNO_2$**, **$CeCoNO_2$**, **Ce@$CoNO_2$**, and **$SmCoNO_2$**. (Table S8) S20

Direct-current (DC) magnetic characteristics of **$NdCoNO_2$** and its magnetically diluted sample of **$Nd@LaCoNO_2$**. (Fig. S10) S21

Direct-current (DC) magnetic characteristics of **$CeCoNO_2$** and its magnetically diluted sample of **$Ce@LaCoNO_2$**. (Fig. S11) S22

Temperature-variable alternate-current (AC) magnetic characteristics for **$NdCoNO_2$** under H_{DC} = 1.5 kOe. (Fig. S12) S23

DC-field-variable alternate-current (AC) magnetic characteristics for **$NdCoNO_2$** at T = 1.8 K. (Fig. S13) S24

Temperature-variable alternate-current (AC) magnetic characteristics for **$CeCoNO_2$** under H_{DC} = 0.4 kOe. (Fig. S14) S25

DC-field-variable alternate-current (AC) magnetic characteristics for **$CeCoNO_2$** at T = 1.8 K. (Fig. S15) S26

Direct-current (DC) magnetic characteristics of **$SmCoNO_2$**. (Fig. S16) S27

Temperature-variable alternate-current (AC) magnetic characteristics for **$SmCoNO_2$** under H_{DC} = 0.2 kOe. (Fig. S17) S28

DC-field-variable alternate-current (AC) magnetic characteristics for **$SmCoNO_2$** at T = 1.8 K. (Fig. S18) S29

Temperature-variable alternate-current (AC) magnetic characteristics for **$Nd@LaCoNO_2$** under H_{DC} = 1.5 kOe. (Fig. S19) S30

Temperature-variable alternate-current (AC) magnetic characteristics for **$Nd@LaCoNO_2$** under H_{DC} = 3.5 kOe. (Fig. S20) S31

DC-field-variable alternate-current (AC) magnetic characteristics for **$Nd@LaCoNO_2$** at T = 1.8 K. (Fig. S21) S32

Temperature-variable alternate-current (AC) magnetic characteristics for **$Ce@LaCoNO_2$** under H_{DC} = 0.4 kOe. (Fig. S22) S33

Temperature-variable alternate-current (AC) magnetic characteristics for **$Ce@LaCoNO_2$** under H_{DC} = 3.5 kOe. (Fig. S23) S34

DC-field-variable alternate-current (AC) magnetic characteristics for **$Ce@LaCoNO_2$** at T = 1.8 K. (Fig. S24) S35

SEM images taken for the selected points or areas of the crystals of **$Nd@LaCoNO_2$** and **$Ce@LaCoNO_2$**, with the indicated probed points/areas that were used for the EDX analysis. (Fig. S25) S36

Results of SEM-EDX microanalyses performed for **$Nd@LaCoNO_2$** and **$Ce@LaCoNO_2$**, including the determined metal ratio for each probed point/area of the crystal and the resulting average values of the metal ratios of the applied lanthanide ions. (Table S9) S37

Best-fit parameters of the field- and temperature-dependencies of magnetic relaxation times of **$NdCoNO_2$**, **$Nd@LaCoNO_2$**, **$CeCoNO_2$**, and **$Ce@LaCoNO_2$**. (Table S10 with the comment related to the measurements and the fitting of AC magnetic data in **$NdCoNO_2$**, **$Nd@LaCoNO_2$**, **$CeCoNO_2$**, and **$Ce@LaCoNO_2$**) S38

Details of the *ab initio* calculations. S39

The expanded molecular fragment of **$LnCoNO_2$** used for the optimization of the positions of H-atoms (a model with additional molecules H-bonded with crucial coordinated water molecules and with La(III) centers placed at the Ln(III) position) and the reduced molecular fragment used for subsequent SA-CASSCF calculations and the simulation of the magnetic properties. (Fig. S26) S40

Description and contractions of the basis set employed in the SA-CASSCF calculations for Ce(III) complexes in **$CeCoNO_2$** and Nd(III) complexes in **$NdCoNO_2$**. (Table S11) S40

Comparison of the *ab initio*-simulated magnetization versus magnetic field curves and the *ab initio*-simulated temperature dependencies of the magnetic susceptibility–temperature product of **$NdCoNO_2$** and **$CeCoNO_2$** with the respective experimental data. (Fig. S27) S41

The results of the *ab initio* calculations for **$CeCoNO_2$**, including the energy splitting of the three SOC doublets in the ground $^2F_{5/2}$ multiplet, their main magnetic axes (pseudo-g-tensor components), and their composition presented in the $|J = 5/2, m_J\rangle$ basis. (Table S12) S42

The results of the *ab initio* calculations for **$NdCoNO_2$**, including the energy splitting of the three SOC doublets in the ground $^4I_{9/2}$ multiplet, their main magnetic axes (pseudo-*g*-tensor components), and their composition presented in the $|J = 9/2, m_J\rangle$ basis. (Table S13) S43

Calculated electric dipole moment vectors for the lanthanide(III) complexes in the **$LnCoNO_2$** series of compounds, compared with the experimental values of their relative SHG intensity. (Table S14) S44

The molecular fragment used for the evaluation of the electric dipole moment vector in relation to the main crystallographic axes of the compounds from the **$LnCoNO_2$** family. (Fig. S28) S44

Solid-state excitation spectra for the monitored indicated Nd(III)-centered emission of ***d*-$NdCoNO_2$** with the broadened spectral range of 2**7**0–900 nm. (Fig. S29) S45

Room-temperature solid-state excitation and emission spectra of the reference compound of $\{[Nd^{III}(OH_2)_3][Co^{III}(CN)_5(NO_2)]\}\cdot 2H_2O$. (Fig. S30) S46

Experimentally determined powder X-ray diffraction pattern of the reference compound of $\{[Nd^{III}(OH_2)_3][Co^{III}(CN)_5(NO_2)]\}\cdot 2H_2O$ compared with the calculated pattern based on the structural model of the previously reported $\{[La^{III}(OH_2)_3][Fe^{III}(CN)_6]\}\cdot 2H_2O$ analog. (Fig. S31) S47

Infrared (IR) absorption spectrum of the reference compound of $\{[Nd^{III}(OH_2)_3][Co^{III}(CN)_5(NO_2)]\}\cdot 2H_2O$ in the range of 4000–600 cm^{-1}. (Fig. S32) S48

Comment to Fig. S29–S32, i.e., on supporting studies aimed at the elucidation of the role of Co(III)-based metalloligands and 4,4'-bpdo ligands in the emission of Nd(III) complexes in **$NdCoNO_2$**. S49

References to the Supporting Information. S50

Experimental section

Materials

$K_3[Co^{III}(CN)_5(NO_2)]$ has been prepared by the modification of the literature procedures,[S1,S2] which have been recently discussed by us.[S3] As presented in Scheme 1 (main text), this synthesis involves, first, the preparation of $[Co^{III}(N_3)(NH_3)]^{3+}$ ion from $Co^{II}Cl_2{\cdot}6H_2O$, which is followed by the cyanation reaction leading to $[Co^{III}(CN)_5(N_3)]^{3-}$ ion. The latter is, at the last step, transformed into the target $[Co^{III}(CN)_5(NO_2)]^{3-}$ ion by the acid-supported substitution of an azido ligand with the nitrito-*κ*N one.[S1–S3] The potassium salt of this ion was isolated and used for the syntheses of the reported compounds.

The organic ligand of 4,4'-bipyridine-*N*,*N*'-dioxide (4,4'-bpdo) has been prepared by the simple oxidation of a commercially available 4,4'-bipyridine precursor, following the modified literature procedure (see below).[S4] The other necessary molecular precursors, including $La^{III}Cl_3{\cdot}7H_2O$ (CAS: 10025-84-0), $Ce^{III}Cl_3{\cdot}7H_2O$ (CAS: 18618-55-8), $Sm^{III}Cl_3{\cdot}6H_2O$ (CAS: 13465-55-9), glacial acetic acid (CAS: 64-19-7), 4,4'-bipyridine (CAS: 553-26-4), $K_3[Fe^{III}(CN)_6]$ (CAS: 13746-66-2), $K_3[Co^{III}(CN)_6]$ (CAS: 13963-58-1) and common solvents, were obtained from Merck or TCI Chemicals. Deuterated solvents, including D_2O (CAS: 7789-20-0) and CD_3OD (CAS: 811-98-3), were purchased from Merck.

Syntheses

Synthesis of 4,4'-bipyridine-*N*,*N*'-dioxide (4,4'-bpdo)

In a round-bottom flask, 4,4'-bipyridine (5.0 g, 32 mmol) was dissolved in 37.5 mL of glacial acetic acid, and 6.5 mL of 30% H_2O_2 solution was added. The solution was heated to 100℃, and after 3 h additional portion of 4.5 mL of the same hydrogen peroxide solution was added. After 24 hours, the solution was cooled down, and 250 mL of acetone was used to precipitate the product. Yellowish needle-like crystals formed immediately. They were dissolved in a minimal amount of distilled water and recrystallized with acetone. Yield: 53.3% (3.21 g).

Synthesis of $LnCoNO_2$, where Ln = La, Ce, Pr, Nd, Sm

In a container suitable for crystallization (7.5 mL vial), 4,4'-bpdo (37.6 mg, 0.20 mmol, 2 eq.) was dissolved in 1.5 mL of distilled water. Then, 0.5 mL of an aqueous solution of a lanthanide salt was added. This includes the solution of $La^{III}Cl_3{\cdot}7H_2O$ (37.1 mg, 0.10 mmol, 1 eq.) for **$LaCoNO_2$**, $Ce^{III}Cl_3{\cdot}7H_2O$ (37.3 mg, 0.10 mmol, 1.0 eq.) for **$CeCoNO_2$**, $Pr^{III}Cl_3{\cdot}7H_2O$ (37.4 mg, 0.10 mmol, 1.0 eq.) for **$PrCoNO_2$**, $Nd^{III}Cl_3{\cdot}6H_2O$ (35.9 mg, 0.10 mmol, 1.0 eq.) for **$NdCoNO_2$**, and $Sm^{III}Cl_3{\cdot}6H_2O$ (36.5 mg, 0.10 mmol, 1.0 eq.) for **$SmCoNO_2$**. To this solution, $K_3[Co^{III}(CN)_5(NO_2)]$ (35.2 mg, 0.10 mmol, 1 eq.) in 0.5 mL water was added. At the end, 0.5 mL of ethanol was added to induce crystallization. After a few hours, platelet crystals of the respective compound from the series of **$LnCoNO_2$** formed. They were washed with water and diethyl ether and dried in the air. They were found to be stable under ambient laboratory conditions (room temperature, air atmosphere). The details of the composition (determined by the CHN elemental analysis and the SC-XRD data) and the synthetic yields for the obtained compounds are given below.

$LaCoNO_2$, i.e., $\{[La^{III}(4,4'\text{-bpdo})_2(OH_2)_4][Co^{III}(CN)_5(NO_2)]\}\cdot 2H_2O$: pale yellow crystals, yield: 66.8% (57.3 mg), CHN elemental analysis calculated: C: 34.98% N: 16.32% H: 3.29%, experimental: C: 34.35% N: 16.12% H: 3.41%.

$CeCoNO_2$, i.e., $\{[Ce^{III}(4,4'\text{-bpdo})_2(OH_2)_4][Co^{III}(CN)_5(NO_2)]\}\cdot 2H_2O$: pale yellow crystals, yield: 71.4% (61.4 mg), CHN elemental analysis calculated: C: 34.93% N: 16.30% H: 3.28%, experimental: C: 34.30% N: 16.01% H: 3.47%.

$PrCoNO_2$, i.e., $\{[Pr^{III}(4,4'\text{-bpdo})_2(OH_2)_4][Co^{III}(CN)_5(NO_2)]\}\cdot 2H_2O$: light green crystals, yield: 66.0% (56.8 mg), CHN elemental analysis calculated: C: 34.90% N: 16.38% H: 3.28%, experimental: C: 34.34% N: 16.16% H: 3.37%.

$NdCoNO_2$, i.e., $\{[Nd^{III}(4,4'\text{-bpdo})_2(OH_2)_4][Co^{III}(CN)_5(NO_2)]\}\cdot 2H_2O$: light pink crystals, yield: 74.1% (64.0 mg), CHN elemental analysis calculated: C: 34.76% N: 16.70% H: 3.27%, experimental: C: 34.55% N: 15.95% H: 3.46%.

$SmCoNO_2$, i.e., $\{[Sm^{III}(4,4'\text{-bpdo})_2(OH_2)_4][Co^{III}(CN)_5(NO_2)]\}\cdot 2H_2O$: pale yellow crystals, yield: 56.3% (49.0 mg), CHN elemental analysis calculated: C: 34.52% N: 16.10% H: 3.24%, experimental: C: 34.13% N: 15.93% H: 3.46%.

The subtly higher-than-expected differences between the calculated and experimental values of the C, H, and N percentages are due to the non-negligible hygroscopic character of the obtained compounds. This leads to the slightly decreased values of the C and N mass percentages and the increased value of the H percentage.

Synthesis of magnetically diluted samples, $Ln@LaCoNO_2$, where Ln = Ce, Nd

Magnetically diluted (with diamagnetic La(III) centers) samples of **$CeCoNO_2$** and **$NdCoNO_2$** were prepared analogously to the compounds described above (**$LnCoNO_2$**). Instead of a single lanthanide precursor, the following mixtures of lanthanide(III) salts were used: (a) for **$Ce@LaCoNO_2$**, $Ce^{III}Cl_3{\cdot}7H_2O$ (3.7 mg, 0.01 mmol, 0.1 eq.) and $La^{III}Cl_3{\cdot}7H_2O$ (33.4 mg, 0.09 mmol, 0.9 eq.), (b) for **$Nd@LaCoNO_2$**, $Nd^{III}Cl_3{\cdot}6H_2O$ (3.6 mg, 0.01 mmol, 0.1 eq.) and $La^{III}Cl_3{\cdot}7H_2O$ (33.4 mg, 0.09 mmol, 0.9 eq.). The details of the composition and the synthetic yields for the obtained

compounds are given below. The compositions, including the key ratio between two different 4f metal centers, were first roughly investigated using the SEM-EDX analysis (S36 and S37). After that, the molar ratios between the lanthanide centers were determined using the ICP-MS method. These results were used here for the composition of the magnetically diluted samples and, further, in the analysis of their magnetic data. It is worth noting that the determined ratios between Ce(III)/La(III) and Nd(III)/La(III) in the respective compounds agree well with the molar ratios used in the synthesis. **Ce@LaCoNO$_2$, i.e., {[La$^{III}_{0.900}$Ce$^{III}_{0.100}$(4,4'-bpdo)$_2$(OH$_2$)$_4$][Co^{III}(CN)$_5$(NO$_2$)]}·2H$_2$O:** pale yellow crystals, yield: 65.7% (56.4 mg). ICP-MS: Ce 10.02(4)% (counting only the 4f metals composition). **Nd@LaCoNO$_2$, i.e., {[La$^{III}_{0.908}$Nd$^{III}_{0.092}$(4,4'-bpdo)$_2$(OH$_2$)$_4$][Co^{III}(CN)$_5$(NO$_2$)]}·2H$_2$O:** pale yellow crystals, yield: 67.5% (58.0 mg). ICP-MS: Nd 9.22(8)% (counting only the 4f metals composition). The good reliability of the determined 4f metals compositions was further supported by the comparison of the DC magnetic characteristics of the diluted and undiluted samples (**NdCoNO$_2$** with **Nd@LaCoNO$_2$**, Fig. S10; **CeCoNO$_2$** with **Ce@LaCoNO$_2$**, Fig. S11).

Synthesis of the deuterated samples of NdCoNO$_2$, i.e., *d*-NdCoNO$_2$

A deuterated sample of **NdCoNO$_2$** was prepared analogously to the compounds described above. Instead of water, D_2O was used, and instead of ethanol, deuterated methanol was used in the same volumes. During filtration, crystals were washed with 5 drops of D_2O and dried with Et_2O. ***d*-NdCoNO$_2$, i.e., {[Nd^{III}(4,4'-bpdo)$_2$(OD$_2$)$_4$][Co^{III}(CN)$_5$(NO$_2$)]}·2D$_2$O:** light pink crystals, yield: 52.2% (45.7 mg) assuming only D_2O is present in the compound.

Synthesis of the reference compounds of LaFeCN and LaCoCN

The reference compounds, containing hexacyanidometallates(III) of Fe(III) (**LaFeCN**) and Co(III) (**LaCoCN**) instead of heteroligand $[Co^{III}(CN)_5(NO_2)]^{3-}$, were prepared as follows. In a container suitable for crystallization (7.5 mL vial), 4,4'-bpdo (37.6 mg, 0.20 mmol, 2 eq.) was dissolved in 1.5 mL of distilled water and mixed with 0.5 mL of aqueous solution of lanthanum(III) chloride, $La^{III}Cl_3·7H_2O$ (37.1 mg, 0.10 mmol, 1 eq.). To this solution, $K_3[Fe^{III}(CN)_6]$ (32.8 mg, 0.10 mmol, 1 eq., for **LaFeCN**) or $K_3[Co^{III}(CN)_6]$ (33.2 mg, 0.10 mmol, 1 eq., for **LaCoCN**) in 0.5 mL of water was added. After the addition of 0.5 mL of ethanol, the solution turned turbid for **LaFeCN**, while the solution for **LaCoCN** became turbid immediately after the addition of $K_3[Co^{III}(CN)_6]$. The brownish-orange elongated block crystals of **LaFeCN** or white powder for **LaCoCN** formed after a few days. The composition of **LaFeCN** of $\{[La^{III}(OH_2)_5(4,4'\text{-bpdo})_2][Fe^{III}(CN)_6]\}·0.5(4,4'\text{-bpdo})·4H_2O$ was determined based on the SC-XRD data, while the composition of LaCoCN was not determined due to the lack of SC-XRD data and the related structural model. It was only checked by the P-XRD that the obtained crystalline phase is different from the reported series of **LnCoNO$_2$** compounds, as well as from **LaFeCN**.

Synthesis of the reference compound of {[Nd^{III}(OH$_2$)$_3$][Co^{III}(CN)$_5$(NO$_2$)]}·2H$_2$O

The reference compound of $\{[Nd^{III}(OH_2)_3][Co^{III}(CN)_5(NO_2)]\}·2H_2O$ (the composition determined from the preliminary SC-XRD measurement, not reported here, and the structural identity to the previously reported $\{[La^{III}(OH_2)_3][Fe^{III}(CN)_6]\}·2H_2O$ analog, Fig. S31)[S39] was synthesized by the stoichiometric mixing of $Nd^{III}Cl_3·6H_2O$ (179.5 mg, 0.5 mmol, 1 eq) and $K_3[Co^{III}(CN)_5(NO_2)]$ (176.2 mg, 0.5 mmol, 1 eq.) in 2.5 mL of distilled water. The resulting mixture was left for slow evaporation in the vial (7.5 mL of volume). After about 2 weeks, light-pink crystals of the $\{[Nd^{III}(OH_2)_3][Co^{III}(CN)_5(NO_2)]\}·2H_2O$ compound appeared. It is important not to evaporate this mixture to dryness to prevent contamination with KCl. Crystals were washed with methanol and dried in the air. Yield: 46.2% (108.4 mg). CHN elemental analysis calculated: C: 12.80% N: 17.91% H: 2.15%, experimental: C: 13.24% N: 18.34% H: 2.00%.

Physicochemical characterization

Single-crystal X-ray diffraction (SC-XRD)

Crystals of the investigated compounds (**LaCoNO$_2$**, **CeCoNO$_2$**, **NdCoNO$_2$**, **PrCoNO$_2$**, **SmCoNO$_2$**, **LaFeCN**) were taken from the respective mother solutions and then covered with Apiezon® M or N grease. Data were collected at 100(2) K, with the cooling ensured by the cryostat Plus CryoStream 800 Plus (Oxford Instruments). The Bruker D8 VENTURE SC-XRD diffractometer, equipped with a microsource IμS 3.0 (Mo Kα) radiation source and PHOTON III detector, was used. Integration, unit cell determination, absorption correction, data reduction, scaling, and solution with the intrinsic phasing method of SHELXT[S5] were performed within the APEX4 package. Additional modelling and refinement were performed with the SHELXL[S6] program within the WinGX software.[S7] Hydrogen atoms were calculated for aromatic rings and found from residual electron density maps for water molecules. The series of restraints was used to maintain the proper geometries of the components, ensuring also the convergence of the refinement procedure. Structural disorder related to one of the cyanido ligands co-occupying the same positions (with partial occupancy) in the structure as a nitrito-*κ*N ligand was modelled with the help of SADI, SIMU, and EADP restraints. Additionally, due to the other structural disorder, especially those related to the two alternative positions of the other cyanido ligand (refined as two possible positions with partial occupancies), some atoms were treated with ISOR restraints. The remaining alerts appearing for the structural data are described in the related CIF files

deposited in the CCDC database (2539318, 2539314, 2539315, 2539319, 2539316, and 2539317 for **$LaCoNO_2$**, **$CeCoNO_2$**, **$NdCoNO_2$**, **$PrCoNO_2$**, **$SmCoNO_2$**, and **LaFeCN**, respectively).

Powder X-ray diffraction (P-XRD)

The powder samples of the obtained compounds were ground and placed inside glass capillaries, which was followed by sealing the filled capillary with paraffin wax. The P-XRD patterns for them were collected using a Bruker D8 Advance ECO diffractometer equipped with a Cu Kα lamp. For comparison, the calculated P-XRD diffractograms were simulated from the SC-XRD data by using the Mercury software.[S8]

Thermogravimetric analysis (TGA)

The polycrystalline samples of the studied compounds were measured in open aluminium-made crucibles. TG data were collected using Netzsch TG209 F1 Libra® thermogravimetric analyzer in a flow of dry nitrogen. Heating from room temperature was performed at a 1 K/min rate.

Scanning electron microscopy with energy dispersive X-ray analysis (SEM-EDX)

The polycrystalline samples were measured with a Hitachi S-4700 scanning electron microscope (SEM) equipped with an EDX spectrometer.

Inductively Coupled Plasma Mass Spectrometry (ICP-MS) studies

Elemental analysis of metals (La, Ce, Nd) in the polycrystalline samples of **$Ln@LaCoNO_2$** (Ln = Ce, Nd) was performed using an Agilent 7700 ICP-MS spectrometer after transferring the metal ions from the solids to the solution using the complexation by an ethylenediaminetetraacetate ($edta^{4-}$) ligand.

Infrared absorption spectroscopy (IR)

The polycrystalline samples were measured on BaF_2 windows with a Thermo Scientific™ Nicolet iN 10 FTIR microscope. The selected crystalline objects were studied in this experiment; however, we checked the repeatability of the results of a few different objects to ensure that the gathered signal corresponds to the bulk sample.

Ultraviolet-visible absorption spectroscopy (UV-vis)

The powder samples were suspended in paraffin oil and measured between quartz plates with a Shimadzu UV-3600i Plus double-beam UV-vis-NIR spectrophotometer at room temperature.

Second harmonic generation (SHG) measurements

The ground powder samples were measured on a custom optical setup using a 1040 nm femtosecond laser as an excitation light source.[S9] Potassium dihydrogen phosphate (KDP) powder was measured as a reference under the same conditions as the studies of the obtained compounds.

UV-vis-NIR spectrofluorometry

The powder samples were measured using an Edinburgh Instruments FS-5 UV-vis-NIR spectrofluorometer equipped with an NIR InGaAs detector. For the studies of the influence of deuteration of water molecules on the photoluminescence, the measurements were performed for the 26 mg portions of the ground powder samples of **$NdCoNO_2$** and ***d*-$NdCoNO_2$**, which were placed inside Norrel's QTZ500 tubes in the SC-70 module equipped with a quartz dewar and a 550 nm low-pass filter at the emission pathway. The measurement conditions were not changed between measurements of both of those samples. Additional photoluminescence (PL) measurements, including the excitation spectra for ***d*-$NdCoNO_2$** for the broadened excitation range (Fig. S29) and the spectra for the reference compound of $\{[Nd^{III}(OH_2)_3][Co^{III}(CN)_5(NO_2)]\}\cdot 2H_2O$ (Fig. S30), were performed on an FLS-1000 UV-vis-NIR spectrofluorometer equipped with a NIR PMT-1700-LN2 detector. The EPR dewar was used for the related PL studies at 77 K, while the Front-Face sample holder was employed for the measurements at room temperature.

Magnetic measurements

All studied powder samples were inserted into polypropylene capsules, covered with paraffin oil, and additionally immobilized by filling the capsule with cotton wool and closing it. The samples in such a capsule were then placed inside the straw with the help of a cotton thread and Kapton® tape. Measurements were performed with a Quantum Design MPMS®3 SQUID magnetometer with EverCool® cryogenic-liquid-free cooling system. The diamagnetic corrections were taken into account.

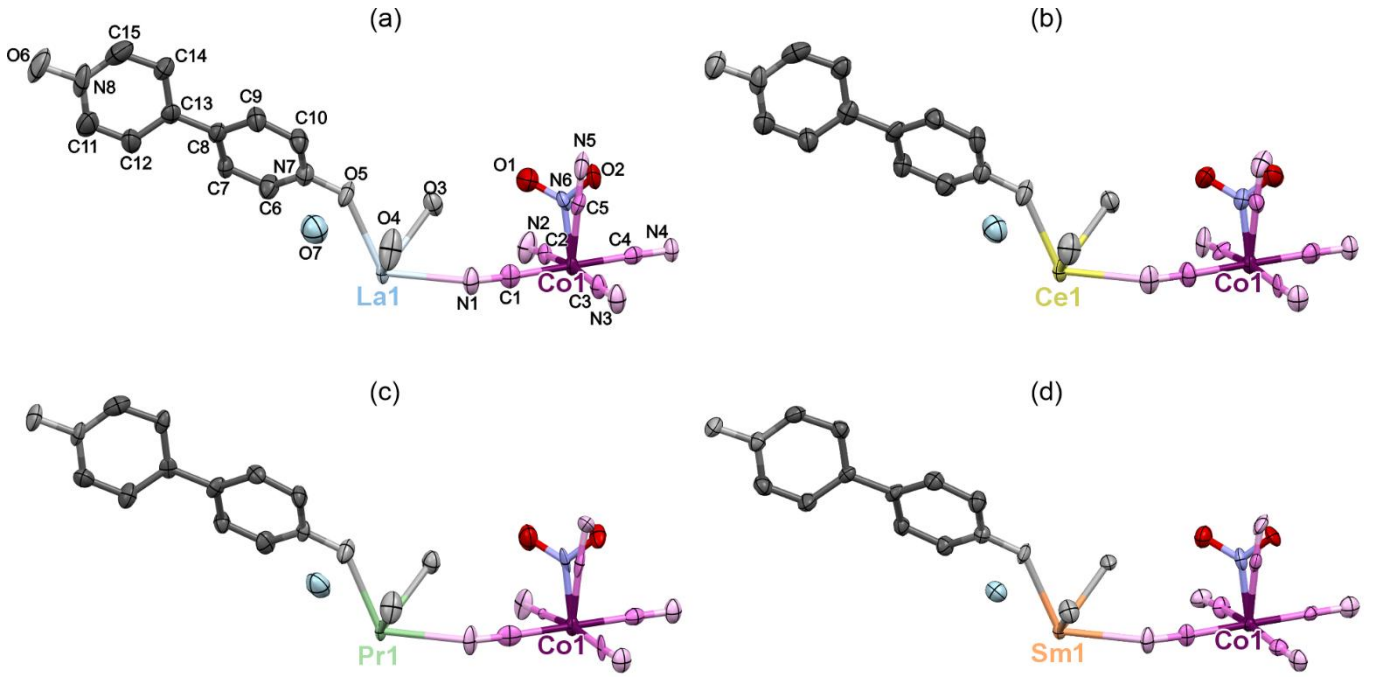

Fig. S1 The asymmetric units of the crystal structures of **$LaCoNO_2$** (a), **$CeCoNO_2$** (b), **$PrCoNO_2$** (c), and **$SmCoNO_2$** (d). See Fig. 1 of the main article for the related view of **$NdCoNO_2$**. Thermal ellipsoids were shown at the 70% probability level. Hydrogen atoms were omitted for clarity. The labelling scheme of all atoms is presented for **$LaCoNO_2$**, while, for the others, only the lanthanide center is labelled, as all other atoms reveal the identical labels as in part (a).

Table S1 Crystal data and structure refinement parameters for **$LaCoNO_2$**, **$CeCoNO_2$**, and **$PrCoNO_2$**.

Compound	$LaCoNO_2$	$CeCoNO_2$	$PrCoNO_2$
Formula	$C_{25}H_{28}LaCoN_{10}O_{12}$	$C_{25}H_{28}CeCoN_{10}O_{12}$	$C_{25}H_{28}PrCoN_{10}O_{12}$
Formula weight / g·mol^{-1}	858.41	859.62	860.41
T / K	100(2)		
λ / Å	0.71073 (Mo Kα)		
Crystal system	orthorhombic	orthorhombic	orthorhombic
Space group	$Cmc2_1$	$Cmc2_1$	$Cmc2_1$
a / Å	22.8817(15)	22.915(5)	22.982(2)
b / Å	7.5829(4)	7.5211(13)	7.5099(7)
c / Å	18.4044(11)	18.353(4)	18.3574(18)
α / °	90	90	90
β / °	90	90	90
γ / °	90	90	90
V / Å^3	3193.3(3)	3163.0(11)	3168.3(5)
Z	4	4	4
ρ_{calc} / g·cm^{-1}	1.786	1.805	1.804
Crystal shape	plate	plate	plate
Crystal size / mm x mm x mm	0.320 x 0.230 x 0.050	0.340 x 0.320 x 0.080	0.550 x 0.250 x 0.020
Absorption coefficient / cm^{-1}	1.917	2.024	2.121
F(000)	1712	1716	1720
ϑ range / °	2.213–25.022	2.219–25.134	2.219–26.022
Limiting indices	-28 < h < 28 -9 < k < 9 -22 < l < 23	-27 < h < 27 -8 < k < 9 -21 < l < 21	-27 < h < 27 -8 < k < 9 -21 < l < 21
Collected reflections	19783	18106	14669
Unique reflections	2893	2815	3148
R_{int}	0.0798	0.1185	0.0654
Completeness / %	99.9	99.5	98.6
Flack parameter	0.026(14)	0.03(2)	0.04(3)
Data/restrains/parameters	2893/17/260	2815/16/260	3146/22/261
GOF on F^2	1.03	1.016	1.101
Final R indices (R_1 for [$I > 2\sigma(I)$] wR_2 for all data)	R_1 = 0.0332 wR_2 = 0.0795	R_1 = 0.0381 wR_2 = 0.0835	R_1 = 0.0405 wR_2 = 0.0818
Largest diff. peak and hole / e·Å^{-3}	1.175/–0.510	1.171/–0.496	0.809/–1.337

Table S2 Crystal data and structure refinement parameters for **$NdCoNO_2$** and **$SmCoNO_2$**.

Compound	$NdCoNO_2$	$SmCoNO_2$
Formula	$C_{25}H_{28}NdCoN_{10}O_{12}$	$C_{25}H_{28}SmCoN_{10}O_{12}$
Formula weight / g·mol^{-1}	863.74	869.85
***T* / K**	100(2)	
***λ* / Å**	0.71073 (Mo Kα)	
Crystal system	orthorhombic	orthorhombic
Space group	$Cmc2_1$	$Cmc2_1$
***a* / Å**	23.0323(11)	23.024(3)
***b* / Å**	7.4716(4)	7.4229(9)
***c* / Å**	18.3614(9)	18.2855(18)
***α* / °**	90	90
***β* / °**	90	90
***γ* / °**	90	90
***V* / Å^3**	3159.8(3)	3125.4(6)
Z	4	4
ρ_{calc} / g·cm^{-1}	1.816	1.849
Crystal shape	plate	plate
Crystal size / mm x mm x mm	0.100 x 0.090 x 0.030	0.210 x 0.180 x 0.030
Absorption coefficient / cm^{-1}	2.228	2.471
***F*(000)**	1724	1732
ϑ range / °	2.837–26.018	2.228–25.026
Limiting indices	-28 < *h* < 28 -9 < *k* < 9 -22 < *l* < 22	-27 < *h* < 27 -8 < *k* < 8 -20 < *l* < 21
Collected reflections	16030	18193
Unique reflections	3183	2768
R_{int}	0.0455	0.0833
Completeness / %	99.9	99.7
Flack parameter	0.03(2)	0.05(2)
Data/restrains/parameters	3183/52/261	2768/28/261
GOF on F^2	1.122	1.004
Final *R* indices (R_1 for [$I > 2\sigma(I)$] wR_2 for all data)	R_1 = 0.0306 wR_2 = 0.0579	R_1 = 0.0319 wR_2 = 0.0748
Largest diff. peak and hole / e·Å^{-3}	0.873/–1.504	1.456/–0.496

Table S3 Selected metric parameters for **$LaCoNO_2$**, **$CeCoNO_2$**, **$PrCoNO_2$**, **$NdCoNO_2$**, and **$SmCoNO_2$**, including the selected bond lengths and angles of lanthanide complexes, as well as the distances between the indicated atoms or moieties representing the main detected supramolecular interactions, i.e., hydrogen bonds and π-π interactions.

Distance / Å	**$LaCoNO_2$**	**$CeCoNO_2$**	**$PrCoNO_2$**	**$NdCoNO_2$**	**$SmCoNO_2$**
Ln1–O5 (O-atom of 4,4'-bpdo)	2.501	2.475	2.468	2.474	2.456
Ln1–O4 (coordinated H_2O)	2.564	2.537	2.535	2.521	2.480
Ln1–O3 (coordinated H_2O)	2.570	2.535	2.523	2.514	2.475
Ln1–N4 (cyanido molecular bridge)	2.615	2.584	2.550	2.559	2.513
Ln1–N3 (cyanido molecular bridge)	2.618	2.582	2.585	2.558	2.540
Ln1–N1 (cyanido molecular bridge)	2.678	2.667	2.644	2.644	2.619
O1–O3 (intralayer H-bond between NO_2^- and coordinated H_2O)	2.898	2.917	2.909	2.916	2.910
O2–O7 (H-bond between NO_2^- and uncoordinated H_2O)	2.843	2.810	2.809	2.801	2.776
O3–O7 (H-bond between coordinated and uncoordinated H_2O)	2.725	2.731	2.753	2.746	2.750
O4–O7 (H-bond between coordinated and uncoordinated H_2O)	2.762	2.755	2.738	2.745	2.748
O6–O7 (H-bond between uncoordinated O-atom of 4,4'-bpdo and uncoordinated H_2O)	2.616	2.640	2.629	2.640	2.647
centroid[N8, C11–C15]–centroid[N8, C11–C15] (representing interlayer π–π interaction between 4,4'-bpdo ligands)	3.856	3.840	3.838	3.822	3.806
centroid[N7, C6–C10]–N5 (representing interlayer π–π interaction between 4,4'-bpdo and cyanido ligands)	3.377	3.379	3.349	3.379	3.376
angle O5–Ln1–O5 (between O-atoms of 4,4'-bpdo ligands coordinated to Ln1 centers)	130°	131°	131°	131°	131°

Table S4 Results of Continuous Shape Measures (CShM) analysis for six-coordinated Co(III) complexes in the **$LnCoNO_2$** series.

Compound: metal center	CShM parameter*					
	HP-6	PPY-6	OC-6	TPR-6	JPPY-6	Geometry
$CeCoNO_2$: Co1	31.206	27.006	**0.355**	13.489	30.645	**OC-6**
$LaCoNO_2$: Co1	31.819	27.396	**0.322**	13.713	30.950	**OC-6**
$NdCoNO_2$: Co1	30.973	27.188	**0.365**	13.567	30.735	**OC-6**
$PrCoNO_2$: Co1	30.709	26.923	**0.366**	13.560	30.559	**OC-6**
$SmCoNO_2$: Co1	31.134	27.910	**0.345**	13.930	31.515	**OC-6**

Table S5 Results of Continuous Shape Measures (CShM) for nine-coordinated lanthanide(III) complexes in the **$LnCoNO_2$** series.

Compound: metal center	CShM parameter*					
	JCSAPR-9	CSAPR-9	JTCTPR-9	TCTPR-9	MFF-9	Geometry
$CeCoNO_2$: Ce1	2.157	0.809	2.384	**0.500**	1.148	**TCTPR-9**
$LaCoNO_2$: La1	2.167	0.805	2.441	**0.524**	1.135	**TCTPR-9**
$NdCoNO_2$: Nd1	2.116	0.805	2.289	**0.512**	1.116	**TCTPR-9**
$PrCoNO_2$: Pr1	2.140	0.800	2.381	**0.535**	1.091	**TCTPR-9**
$SmCoNO_2$: Sm1	2.078	0.805	2.192	**0.509**	1.113	**TCTPR-9**

*Continuous Shape Measures (CShM) parameters:[S10–S12]

six-coordinated complexes

CShM HP-6 – the parameter corresponding to the hexagon (D_{6h} symmetry)
CShM PPY-6 – the parameter corresponding to the pentagonal pyramid (C_{5v})
CShM OC-6 – the parameter corresponding to the octahedron (O_h)
CShM TPR-6 – the parameter corresponding to the trigonal prism (D_{3h})
CShM JPPY-6 – the parameter corresponding to the Johnson pentagonal pyramid (C_{5v})

nine-coordinated complexes

CShM JCSAPR-9 – the parameter corresponding to the Johnson capped square antiprism (C_{4v})
CShM CSAPR-9 – the parameter corresponding to the capped square antiprism (C_{4v})
CShM JTCTPR-9 – the parameter corresponding to the Johnson tricapped trigonal prism (D_{3h})
CShM TCTPR-9 – the parameter corresponding to the tricapped trigonal prism (D_{3h})
CShM MFF-9 – the parameter corresponding to the Muffin (C_s)

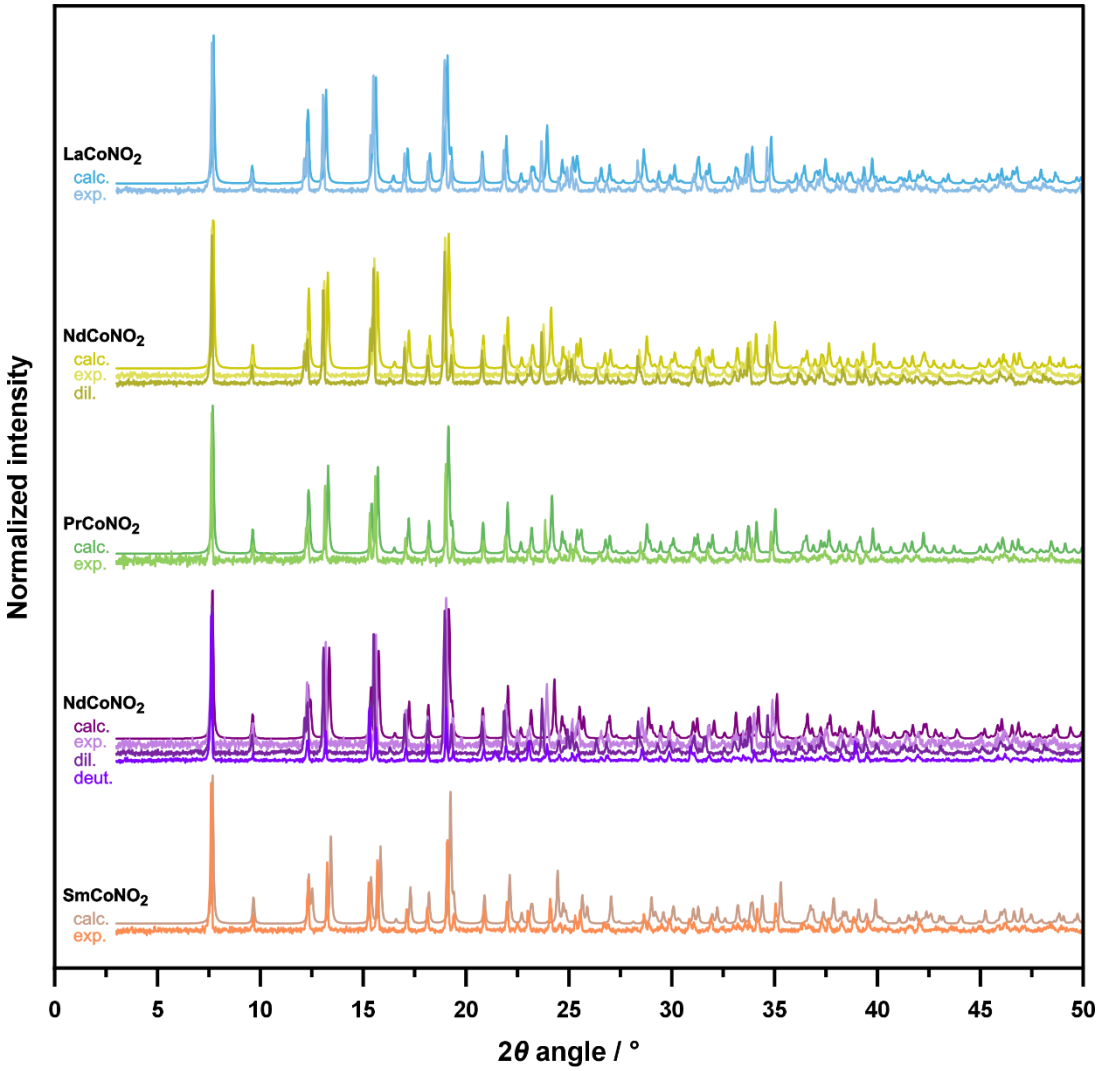

Fig. S2 Powder X-ray diffraction (P-XRD) patterns of **$LaCoNO_2$**, **$CeCoNO_2$**, **$PrCoNO_2$**, **$NdCoNO_2$**, and **$SmCoNO_2$**, including the experimental ones (exp.), the calculated ones based on the respective structural models from the SC-XRD experiments (calc.), as well as the experimental P-XRD patterns for the magnetically diluted compounds of **Ce@$LaCoNO_2$** and **Nd@$LaCoNO_2$** (dil.), and the deuterated compound of ***d*-$NdCoNO_2$** (deut.).

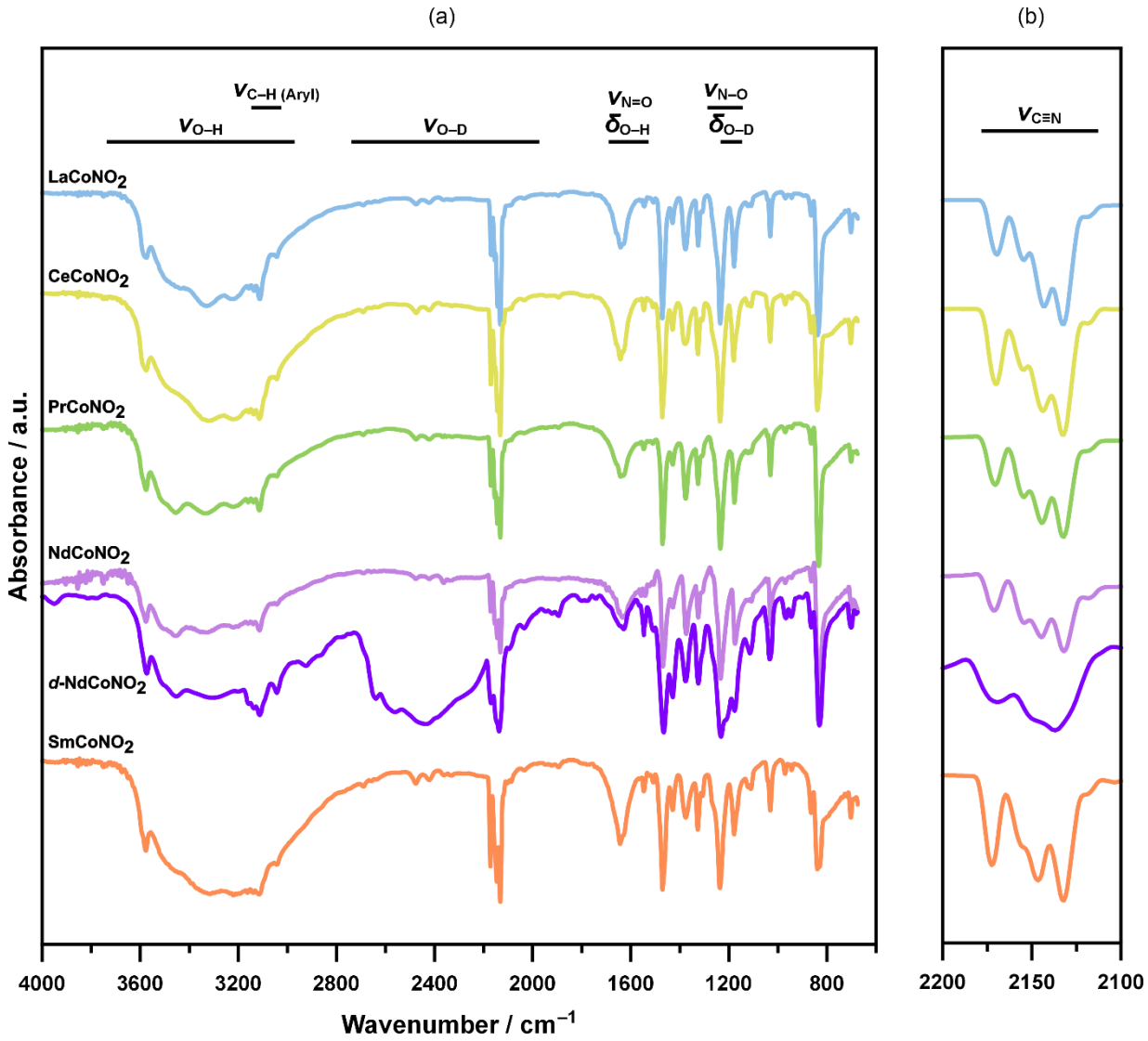

Fig. S3 Infrared (IR) absorption spectra of **$LaCoNO_2$**, **$CeCoNO_2$**, **$PrCoNO_2$**, **$NdCoNO_2$**, ***d*-$NdCoNO_2$**, and **$SmCoNO_2$**, including the broader range of 4000–600 cm^{-1} (a) and the enlarged region of 2200–2100 cm^{-1} (b), corresponding to the cyanido stretching vibrations within the polycyanidometallate linkers.[S13]

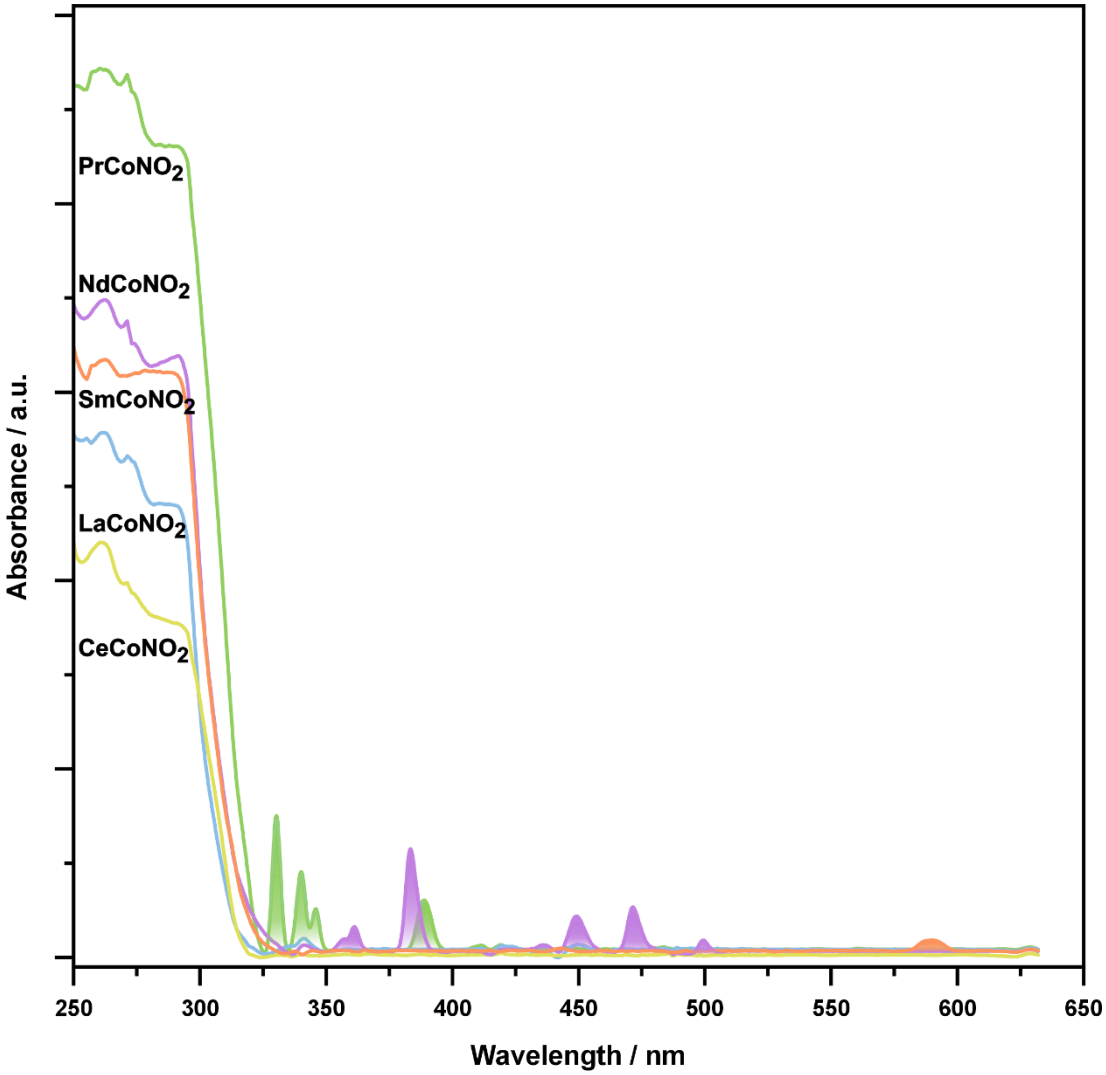

Fig. S4 Solid-state UV-vis absorption spectra for the powder samples of **$LaCoNO_2$**, **$CeCoNO_2$**, **$PrCoNO_2$**, **$NdCoNO_2$**, and **$SmCoNO_2$**. The spectra were re-scaled to show the similarity between the compounds in the UV range, while emphasizing also the f-f electronic transitions that are visible for **$PrCoNO_2$**, **$NdCoNO_2$**, and **$SmCoNO_2$** in the UV-to-vis region.

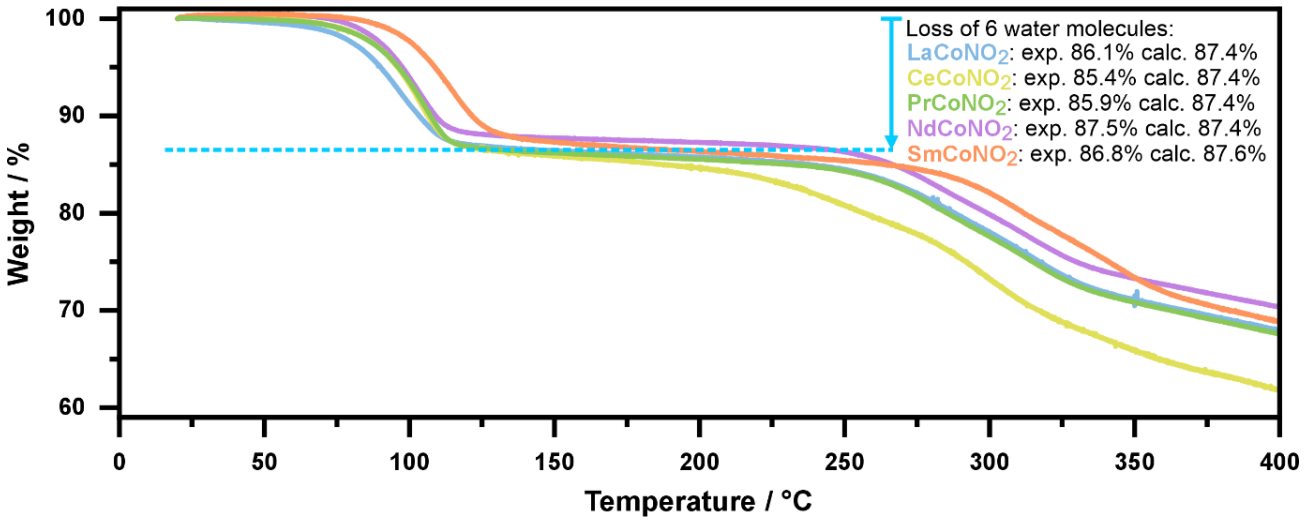

Fig. S5 Thermogravimetric (TG) curves for the powder samples of **$LaCoNO_2$**, **$CeCoNO_2$**, **$PrCoNO_2$**, **$NdCoNO_2$**, and **$SmCoNO_2$**, measured from room temperature to 400 °C. The main heating-induced decrease in the samples' weight in the 80–120 °C range was marked and described by the indicated loss of 6 water molecules per formula unit. The related experimental values of this weight decrease, as well as the calculated values based on the determined composition of the compounds (see Experimental section for the details regarding the composition of the obtained compounds), were indicated.

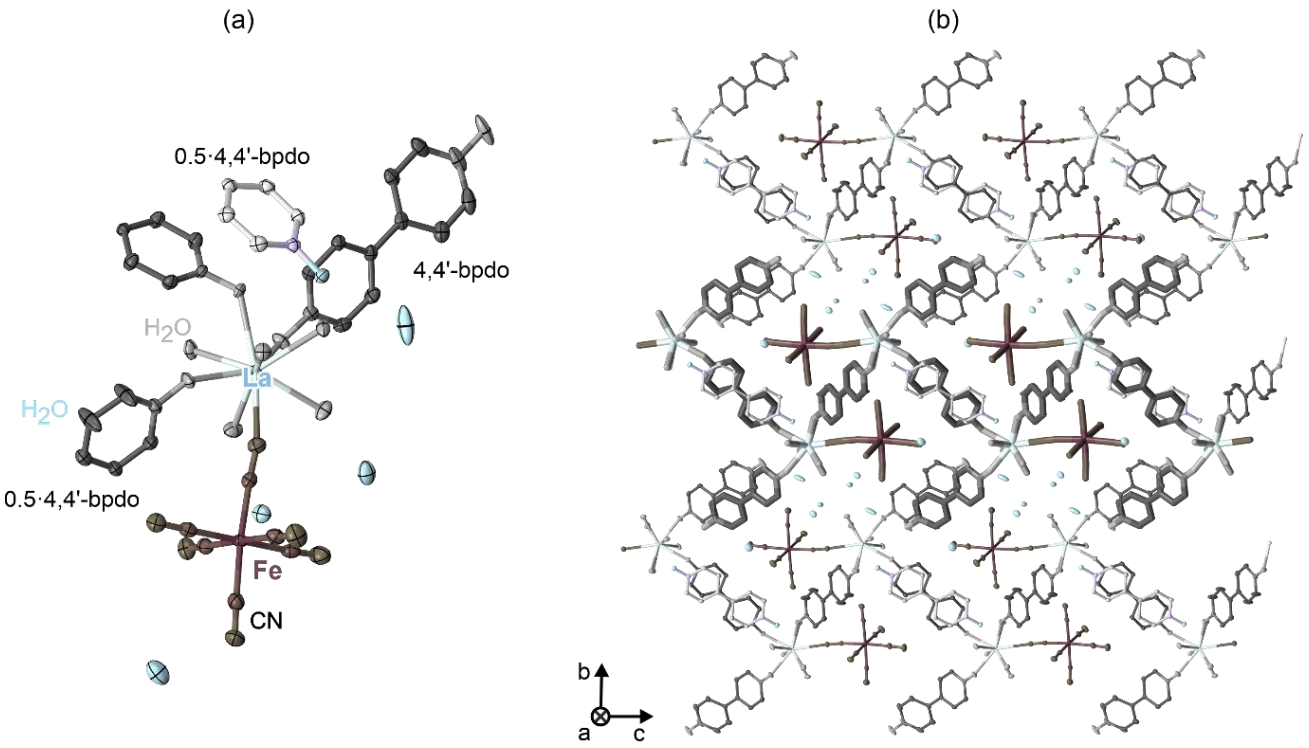

Fig. S6 Representative views of the crystal structure of the reference compound of **LaFeCN**, including its asymmetric unit with the molecular components indicated (a) and the view along within the *bc* plane showing the 1-D coordination skeleton of this compound (one of the presented chains is emphasized by bold sticks), very different from the investigated compounds of **$LnCoNO_2$** (b). Thermal ellipsoids in (a) part were shown at the 70% probability level. Hydrogen atoms were omitted for clarity.

Table S6 Crystal data and structure refinement parameters for the crystal structure of the reference compound of **LaFeCN**.

Compound	LaFeCN
Formula	$C_{31}H_{38}LaFeN_{11}O_{14}$
Formula weight / g·mol^{-1}	983.48
T / K	100(2)
λ / Å	0.71073 (Mo Kα)
Crystal system	triclinic
Space group	$P\overline{1}$
a / Å	8.3559(5)
b / Å	15.4235(9)
c / Å	15.5022(9)
α / °	84.917(2)
β / °	81.060(2)
γ / °	86.033(2)
V / Å^3	1962.7(2)
Z	2
ρ_{calc} / g·cm^{-1}	1.664
Crystal shape	block
Crystal size / mm x mm x mm	0.165 x 0.080 x 0.033
Absorption coefficient / cm^{-1}	1.522
F(000)	992
ϑ range / °	1.955–30.515
Limiting indices	-11 < h < 11 -22 < k < 22 -22 < l < 22
Collected reflections	50311
Unique reflections	11933
R_{int}	0.0571
Completeness / %	99.6
Data/restrains/parameters	11933/18/595
GOF on F^2	1.037
Final R indices (R_1 for [$I > 2\sigma(I)$] wR_2 for all data)	R_1 = 0.0333 wR_2 = 0.0669
Largest diff. peak and hole / e·Å^{-3}	0.594/–0.634

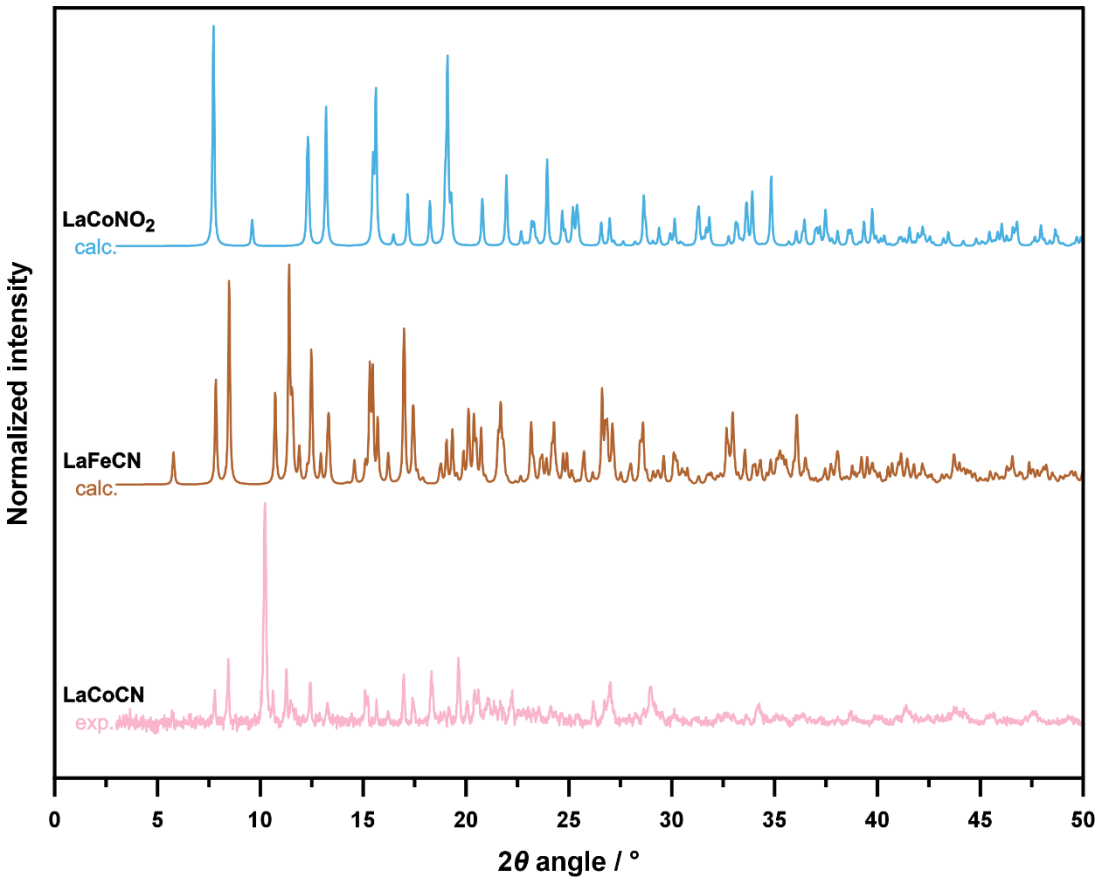

Fig. S7 Comparison of the calculated (based on the SC-XRD data) powder X-ray diffraction (P-XRD) patterns of **$LaCoNO_2$** and **LaFeCN**, as well as the experimental P-XRD pattern for the powder sample of **LaCoCN**, for which the reliable SC-XRD could not be gathered due to the low quality of the single crystals. This comparison indicates that the **LaCoCN** solid is not isostructural to **$LaCoNO_2$**, and most probably it contains a mixture of the phase isostructural to **LaFeCN** and another unknown one.

Table S7 Results of the fitting of the SHG intensity dependence on laser power (x) to a quadratic function for each compound from the **$LnCoNO_2$** series and for the KDP reference. See Fig. 2 for the related best-fit curves. The R^2 parameters of the obtained fits are also provided here.

Compound	Equation with the best-fit parameter	R^2
$CeCoNO_2$	$2278(19)\cdot x^2$	0.99939
$LaCoNO_2$	$2545(20)\cdot x^2$	0.99949
$NdCoNO_2$	$2035(19)\cdot x^2$	0.99925
$PrCoNO_2$	$2783(29)\cdot x^2$	0.99910
$SmCoNO_2$	$2344(23)\cdot x^2$	0.99917
KDP	$2717(25)\cdot x^2$	0.99931

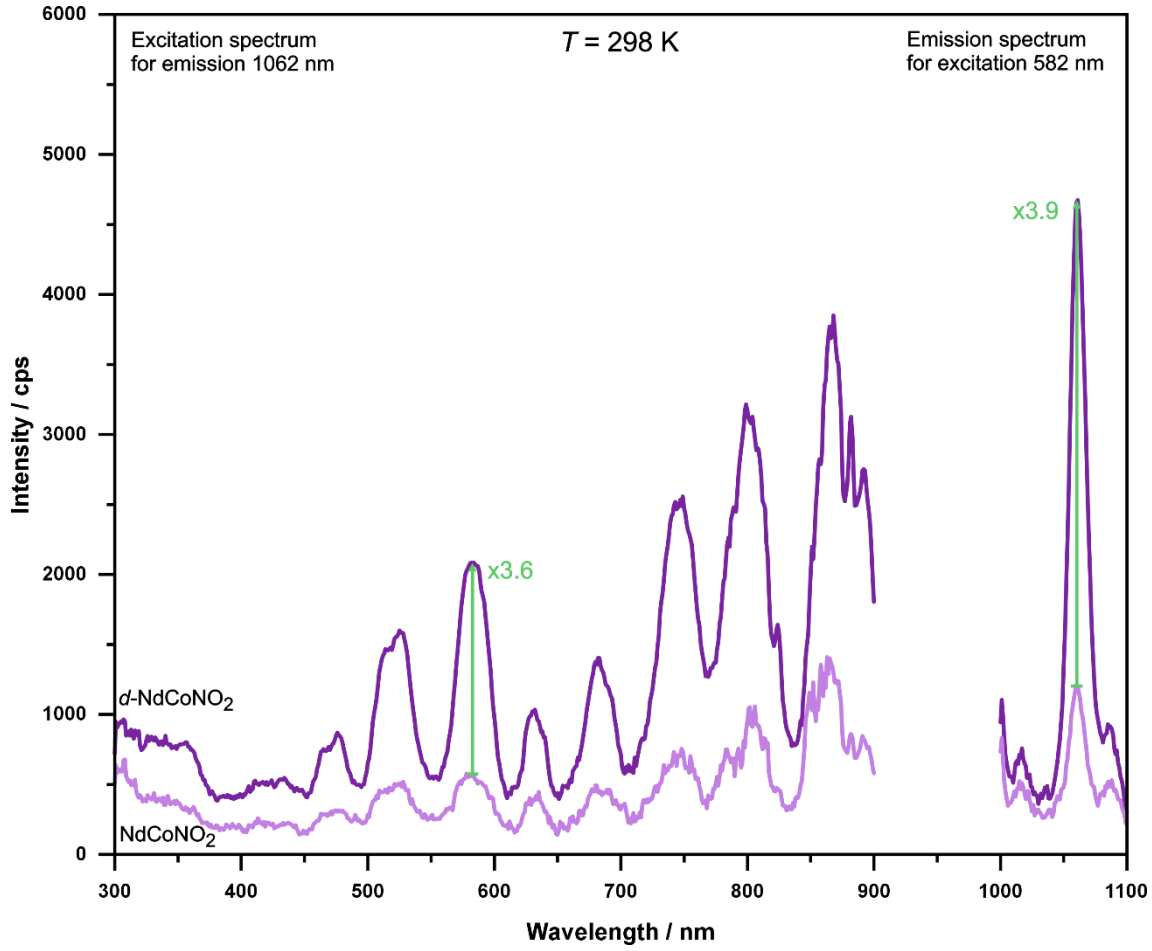

Fig. S8 Room-temperature solid-state emission (right side) and excitation (left side) spectra of **$NdCoNO_2$** and its deuterated sample of ***d*-$NdCoNO_2$**, both measured under identical experimental conditions with the same amount of the sample (see Experimental section for details). Green arrows and accompanying labels show how many times the signal for the deuterated sample is stronger than that for the original compound. The analogous spectra were also gathered at 77 K, see Fig. 2 for comparison.

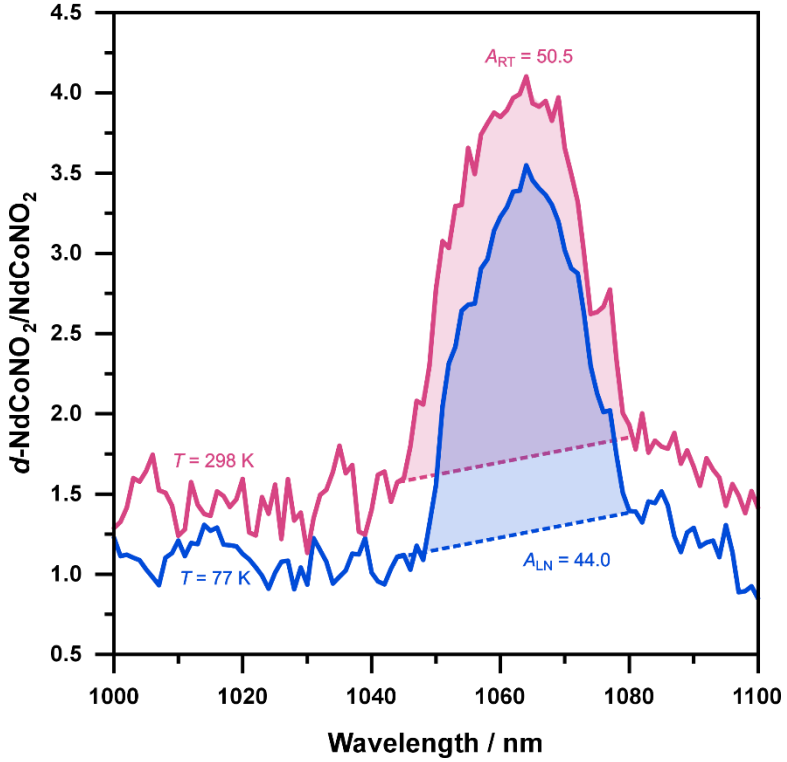

Fig. S9 Wavelength dependences of the ratio between the emission intensities gathered under the 582 excitation for ***d*-NdCoNO$_2$** and **NdCoNO$_2$** (indicated in the *y*-scale as ***d*-NdCoNO$_2$/NdCoNO$_2$**) at room temperature (RT, 298 K) and at the liquid nitrogen temperature (LN, 77 K). The areas below the peak in the 1040–1080 nm range for RT and LN were indicated, and the values of the related surface areas of these peaks are provided.

Table S8 Sample masses used for the SQUID magnetometry measurements, and the diamagnetic corrections employed in the analysis of the gathered raw magnetic data for **NdCoNO$_2$**, **Nd@LaCoNO$_2$**, **CeCoNO$_2$**, **Ce@CoNO$_2$**, and **SmCoNO$_2$**.

NdCoNO$_2$	Nd@LaCoNO$_2$	CeCoNO$_2$	Ce@LaCoNO$_2$	SmCoNO$_2$
Diamagnetic correction / 10^{-6}cm^{3}mol^{-1}				
230	100	110	70	100
Sample mass / mg				
18.6	18.3	20.6	22.3	20.9

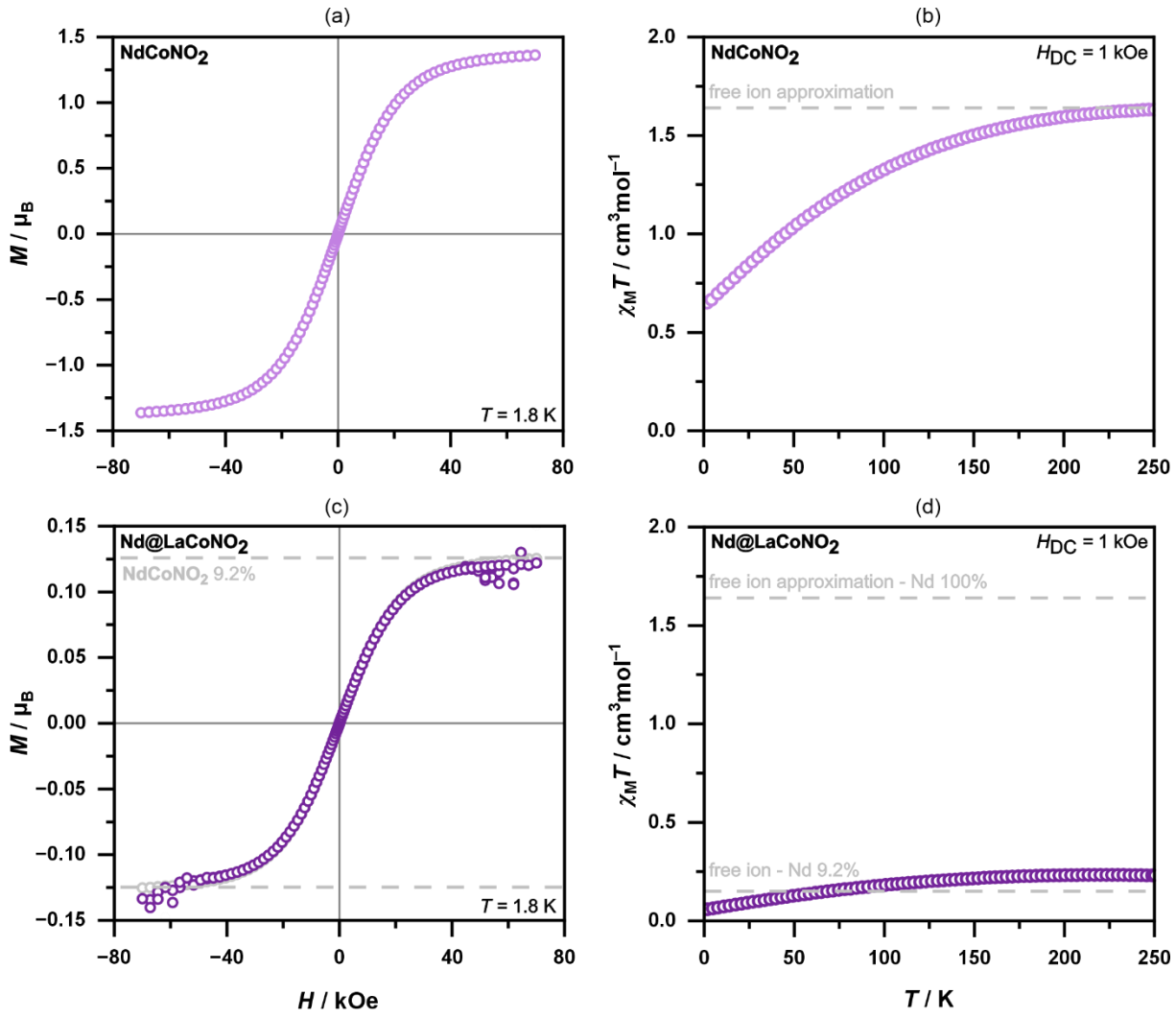

Fig. S10 Direct-current (DC) magnetic characteristics of **$NdCoNO_2$** (a, b) and its magnetically diluted sample of **Nd@$LaCoNO_2$** (c, d), including the magnetization versus magnetic field curves at 1.8 K (a, c) and the temperature dependencies of the magnetic susceptibility–temperature products under H_{DC} = 1 kOe (b, d). The experimental points are shown as light violet empty circles in (a, b) and darker violet empty circles in (c, d). Moreover, in the (c) part that represents the properties of **Nd@$LaCoNO_2$**, the magnetization curves of **$NdCoNO_2$** scaled by the determined content of paramagnetic centers (by ICP-MS, see Experimental section; i.e., 9.2% of Nd(III) centers and 90.8% of La(III) centers on the lanthanide positions of the material) was shown in the background as gray empty circles, while the high-field limits were additionally marked by gray dashed lines. Both the shape of this scaled curve, as well as the related high-field limits, correspond perfectly to the experimental curve of **Nd@$LaCoNO_2$**, additionally confirming the determined 4f metals composition. On the other hand, in the (b) and (d) parts, the magnetic signal level corresponding to the free-ion Nd(III) approximation was indicated by gray dashed lines and labeled.[S13] Moreover, in the (d) part, this approximate signal level was scaled by the determined content of Nd(III) centers for a better comparison with the presented experimental curve of **Nd@$LaCoNO_2$**. The obtained experimental values are close to these limits at high temperature, confirming the validity of the experiments, the presence of Nd(III) centers as the source of paramagnetism, and supporting the results of the ICP-MS-based determination of the 4f metals composition in **Nd@$LaCoNO_2$**.

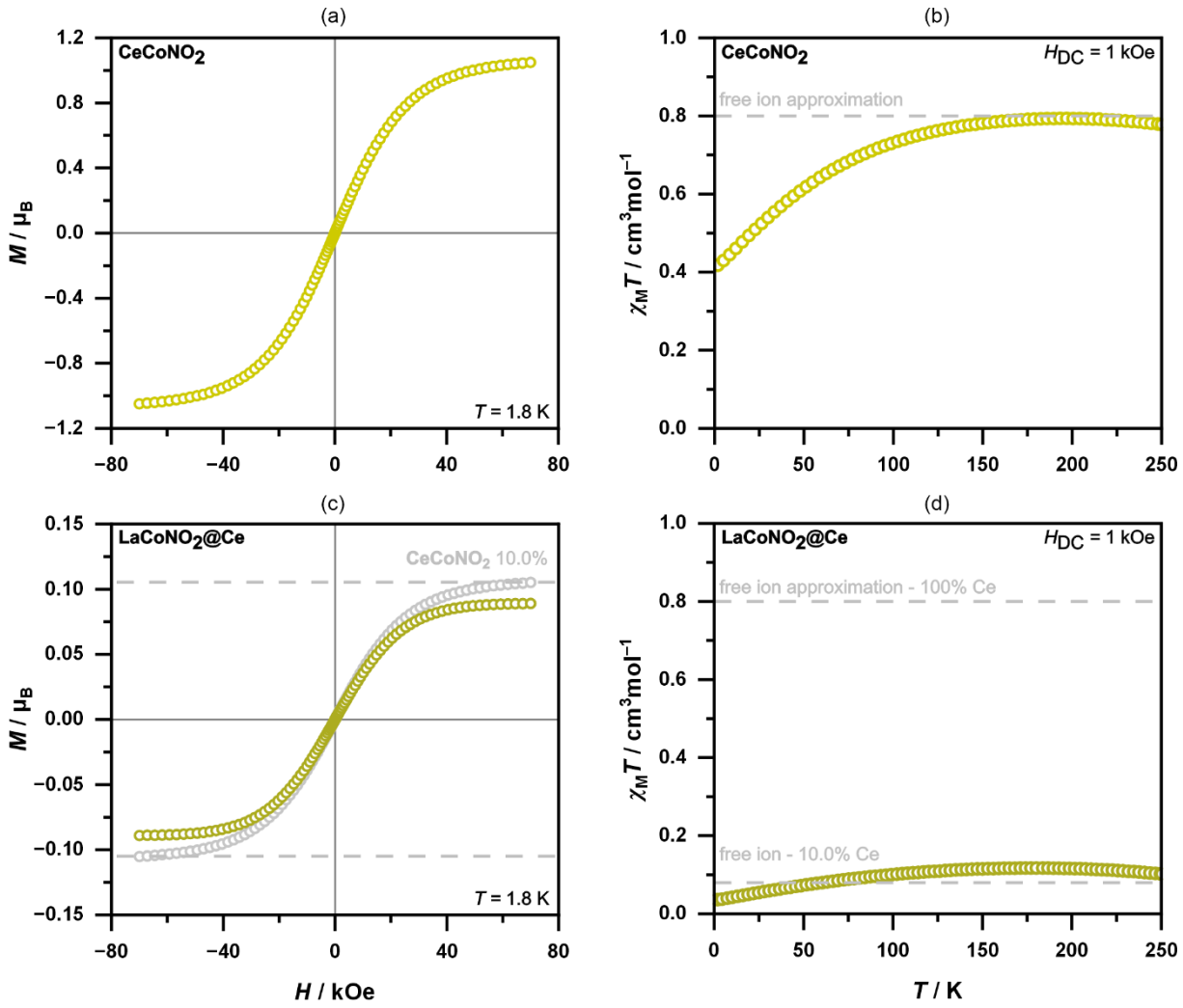

Fig. S11 Direct-current (DC) magnetic characteristics of **$CeCoNO_2$** (a, b) and its magnetically diluted sample of **Ce@$LaCoNO_2$** (c, d), including the magnetization versus magnetic field curves at 1.8 K (a, c) and the temperature dependencies of the magnetic susceptibility–temperature products under H_{DC} = 1 kOe (b, d). The experimental points are shown as light green empty circles in (a, b) and darker green empty circles in (c, d). Moreover, in the (c) part that represents the properties of **Ce@$LaCoNO_2$**, the magnetization curves of **$CeCoNO_2$** scaled by the determined content of paramagnetic centers (by ICP-MS, see Experimental section; i.e., 10.0% of Nd(III) centers and 90.0% of La(III) centers on the lanthanide positions of the material) was shown in the background as gray empty circles, while the high-field limits were additionally marked by gray dashed lines. Both the shape of this scaled curve, as well as the related high-field limits, correspond reasonably to the experimental curve of **Ce@$LaCoNO_2$**, additionally confirming the determined 4f metals composition. On the other hand, in the (b) and (d) parts, the magnetic signal level corresponding to the free-ion Ce(III) approximation was indicated by gray dashed lines and labeled.[S14] Moreover, in the (d) part, this approximate signal level was scaled by the determined content of Ce(III) centers for a better comparison with the presented experimental curve of **Ce@$LaCoNO_2$**. The obtained experimental values are close to these limits at high temperature, confirming the validity of the experiments, the presence of Ce(III) centers as the source of paramagnetism, and supporting the results of the ICP-MS-based determination of the 4f metals composition in **Ce@$LaCoNO_2$**.

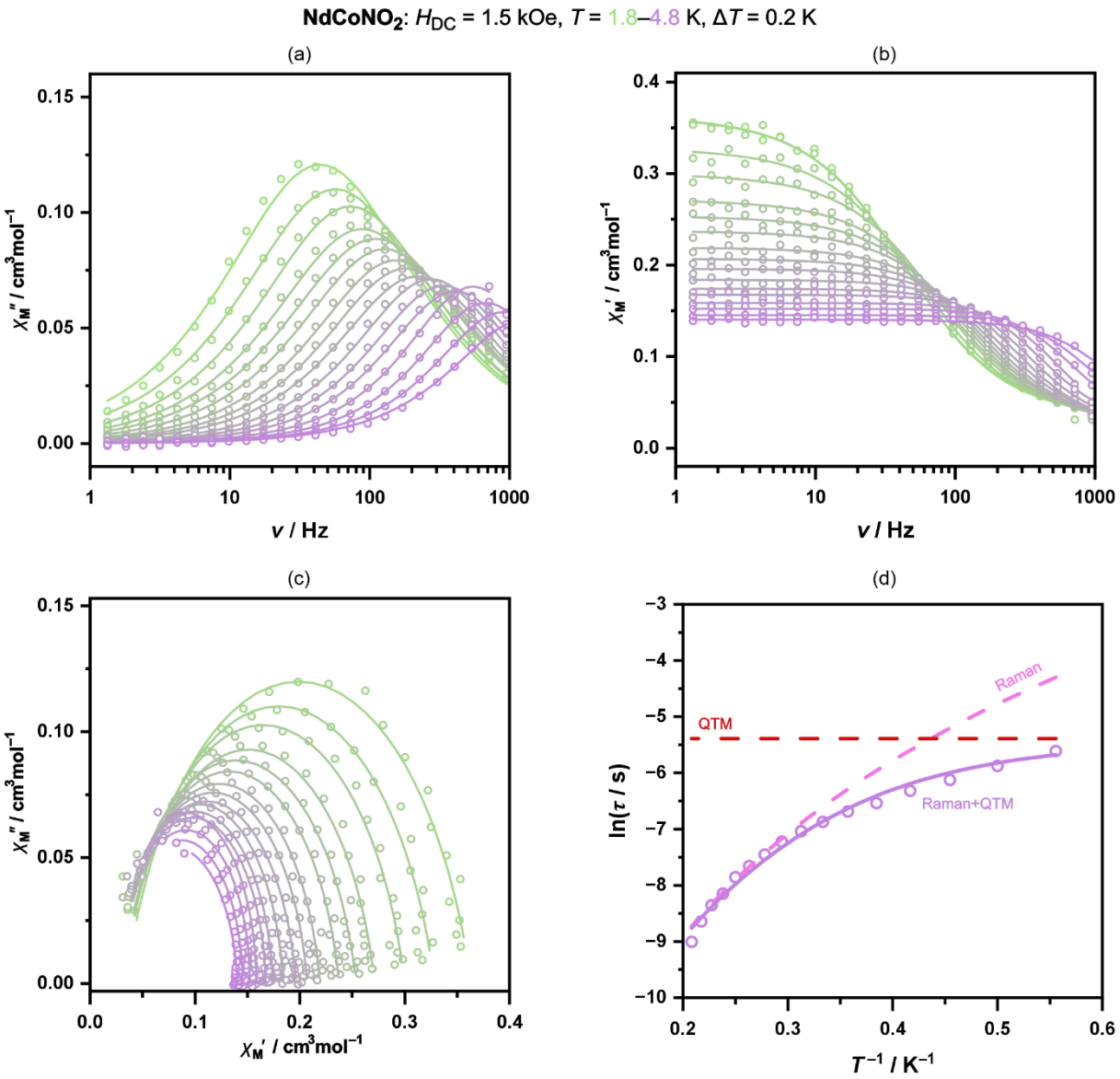

Fig. S12 Temperature-variable alternate-current (AC) magnetic characteristics for **$NdCoNO_2$** under H_{DC} = 1.5 kOe, including the frequency dependencies of the imaginary part of complex AC susceptibility (a), the frequency dependencies of the real part of complex AC susceptibility (b), the related Argand plots (c), and the temperature dependence of the resulting magnetic relaxation times (d). For the (a, b, c) parts, the best fits to the generalized Debye model of a single relaxation process were shown as solid lines. For the (d) part, a solid line represents the best-fit curve obtained using the combined contributions from QTM and Raman processes, while dashed lines represent the separate contributions from the indicated processes. Note that the fit presented in the (d) part was performed as a simultaneous one with the related DC-field dependence of relaxation times, which was realized using the relACs software.[S15]

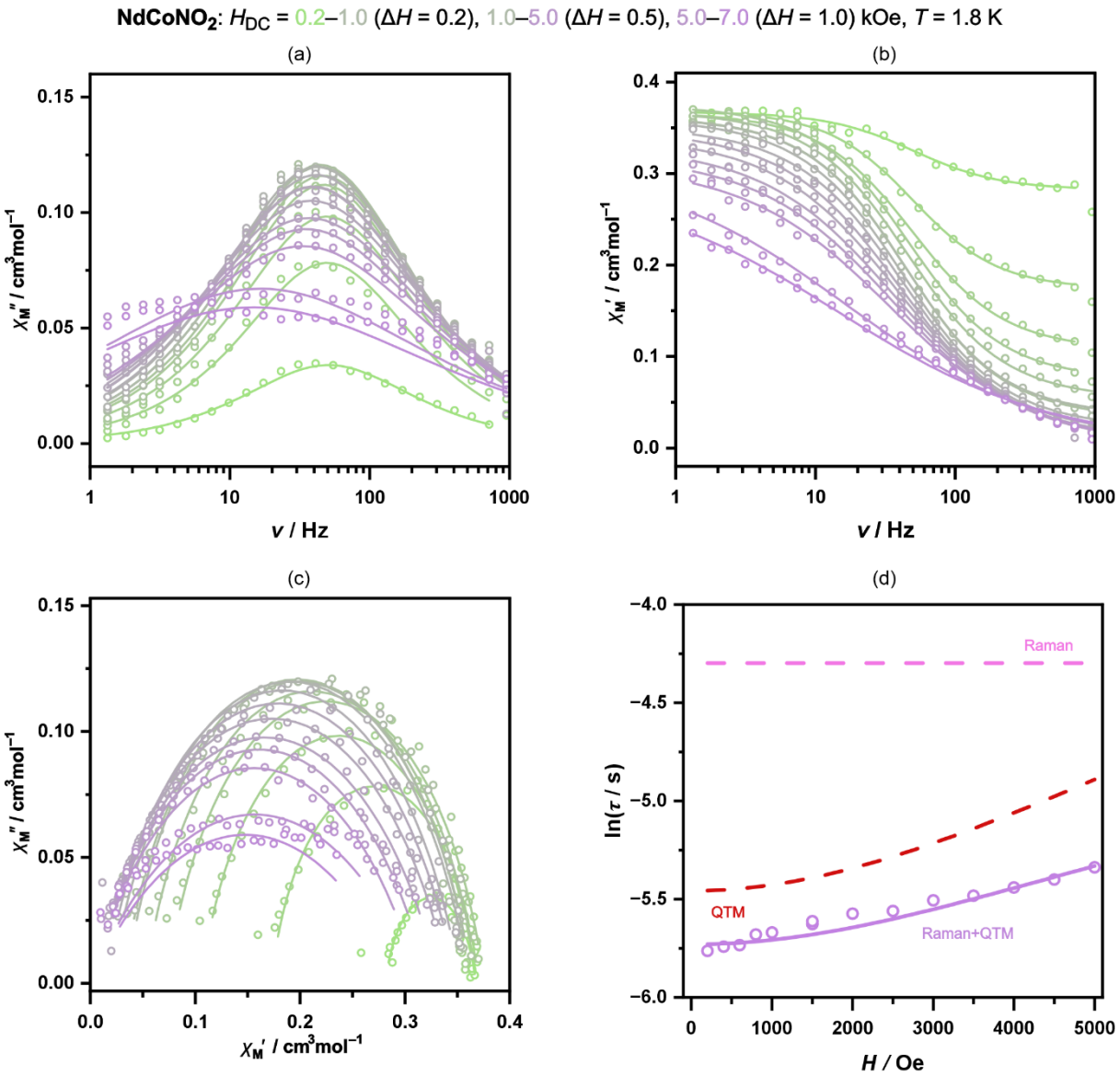

Fig. S13 DC-field-variable alternate-current (AC) magnetic characteristics for **$NdCoNO_2$** at T = 1.8 K, including the frequency dependencies of the imaginary part of complex AC susceptibility (a), the frequency dependencies of the real part of complex AC susceptibility (b), the related Argand plots (c), and the DC-field dependence of the resulting magnetic relaxation times (d). For the (a, b, c) parts, the best fits to the generalized Debye model of a single relaxation process were shown as solid lines. For the (d) part, a solid line represents the best-fit curve obtained using the combined contributions from QTM and Raman processes, while dashed lines represent the separate contributions from the indicated processes. Note that the fit presented in the (d) part was performed as a simultaneous one with the related temperature dependence of relaxation times, which was realized using the relACs software.[S15]

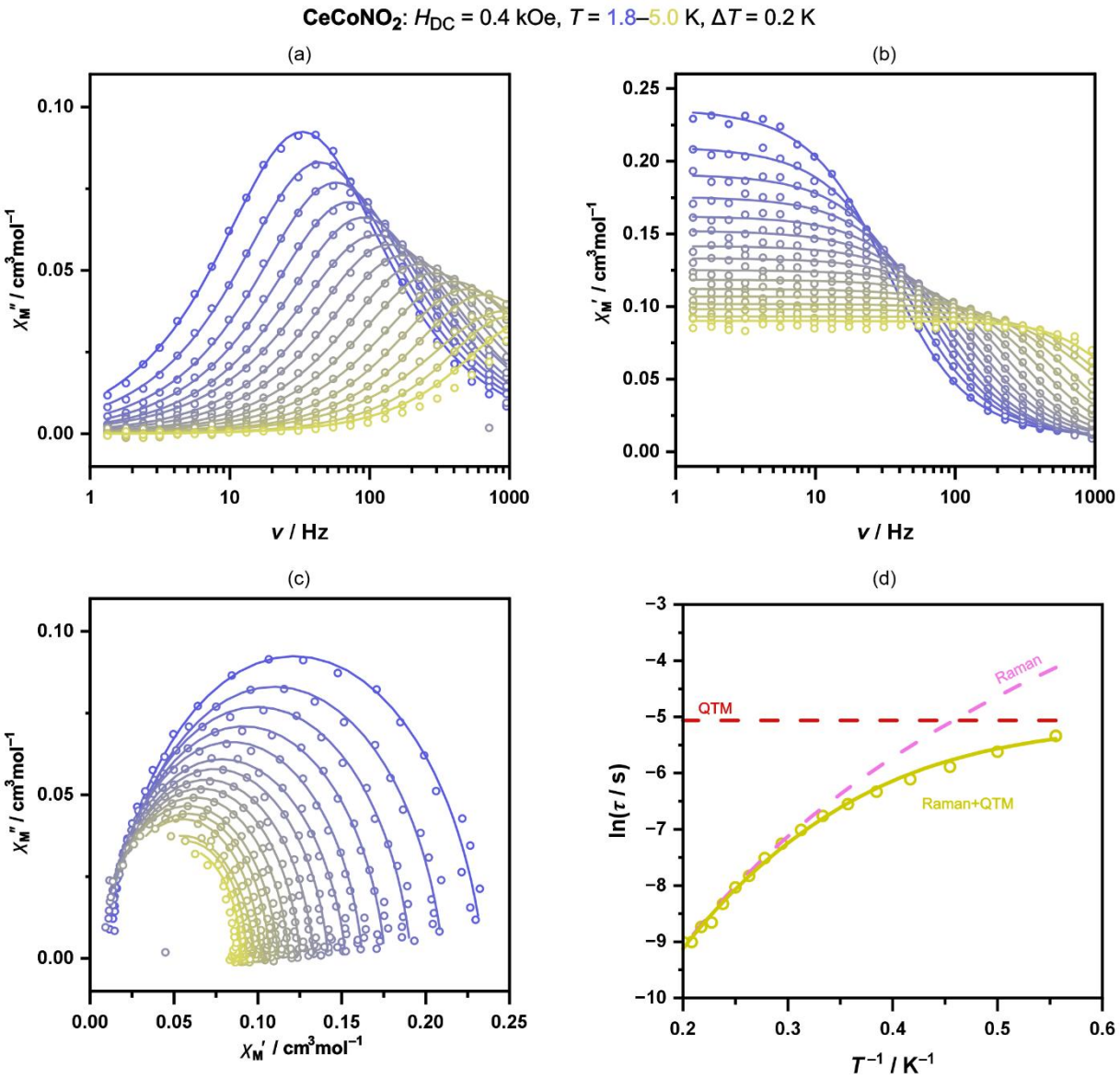

Fig. S14 Temperature-variable alternate-current (AC) magnetic characteristics for **$CeCoNO_2$** under H_{DC} = 0.4 kOe, including the frequency dependencies of the imaginary part of complex AC susceptibility (a), the frequency dependencies of the real part of complex AC susceptibility (b), the related Argand plots (c), and the temperature dependence of the resulting magnetic relaxation times (d). For the (a, b, c) parts, the best fits to the generalized Debye model of a single relaxation process were shown as solid lines. For the (d) part, a solid line represents the best-fit curve obtained using the combined contributions from QTM and Raman processes, while dashed lines represent the separate contributions from the indicated processes. Note that the fit presented in the (d) part was performed as a simultaneous one with the related DC-field dependence of relaxation times, which was realized using the relACs software.[S15]

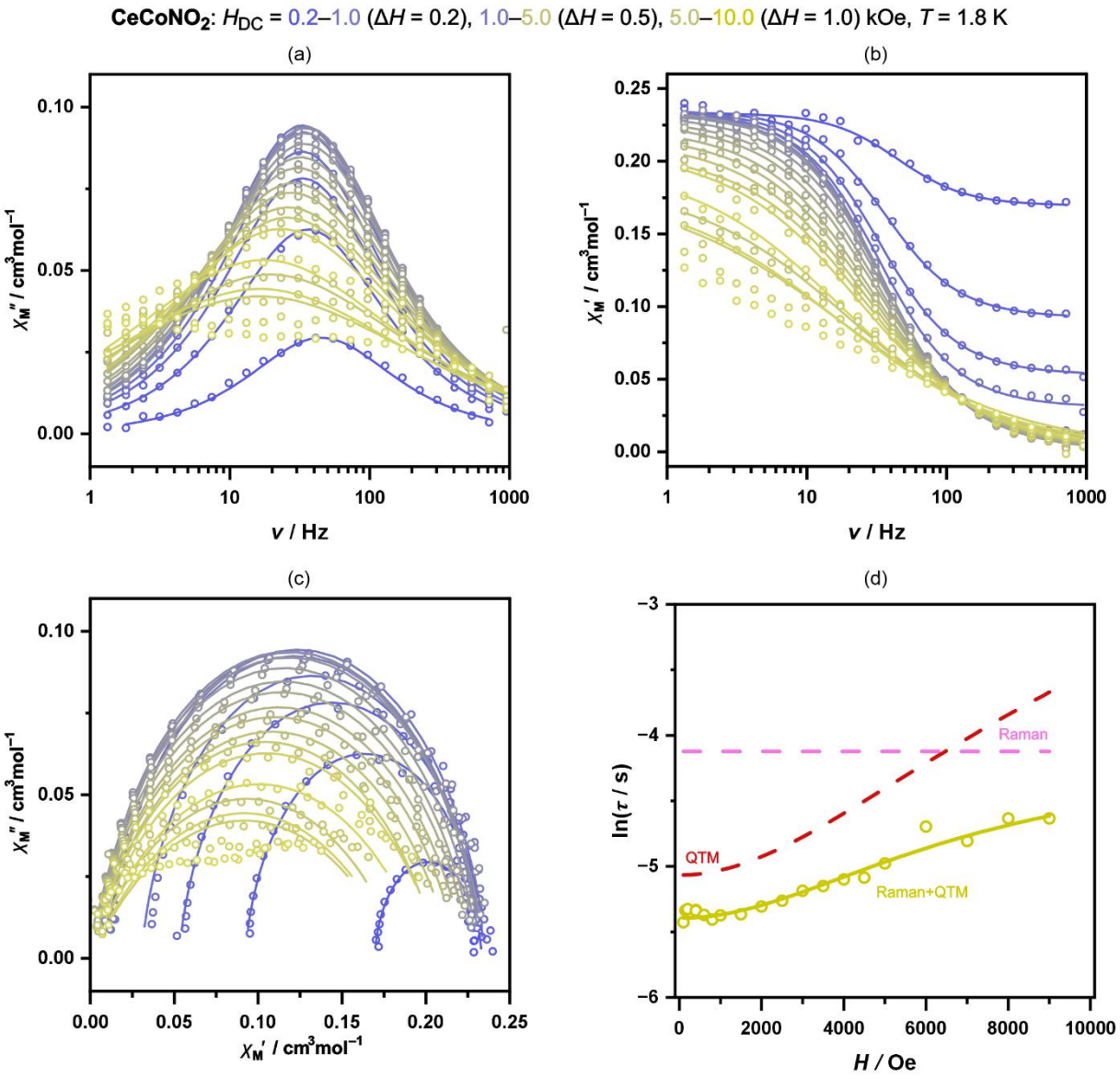

Fig. S15 DC-field-variable alternate-current (AC) magnetic characteristics for **$CeCoNO_2$** at T = 1.8 K, including the frequency dependencies of the imaginary part of complex AC susceptibility (a), the frequency dependencies of the real part of complex AC susceptibility (b), the related Argand plots (c), and the DC-field dependence of the resulting magnetic relaxation times (d). For the (a, b, c) parts, the best fits to the generalized Debye model of a single relaxation process were shown as solid lines. For the (d) part, a solid line represents the best-fit curve obtained using the combined contributions from QTM, Raman, and Direct processes, while dashed lines represent the separate contributions from the indicated processes. Note that the fit presented in the (d) part was performed as a simultaneous one with the related temperature dependence of relaxation times, which was realized using the relACs software.[S15]

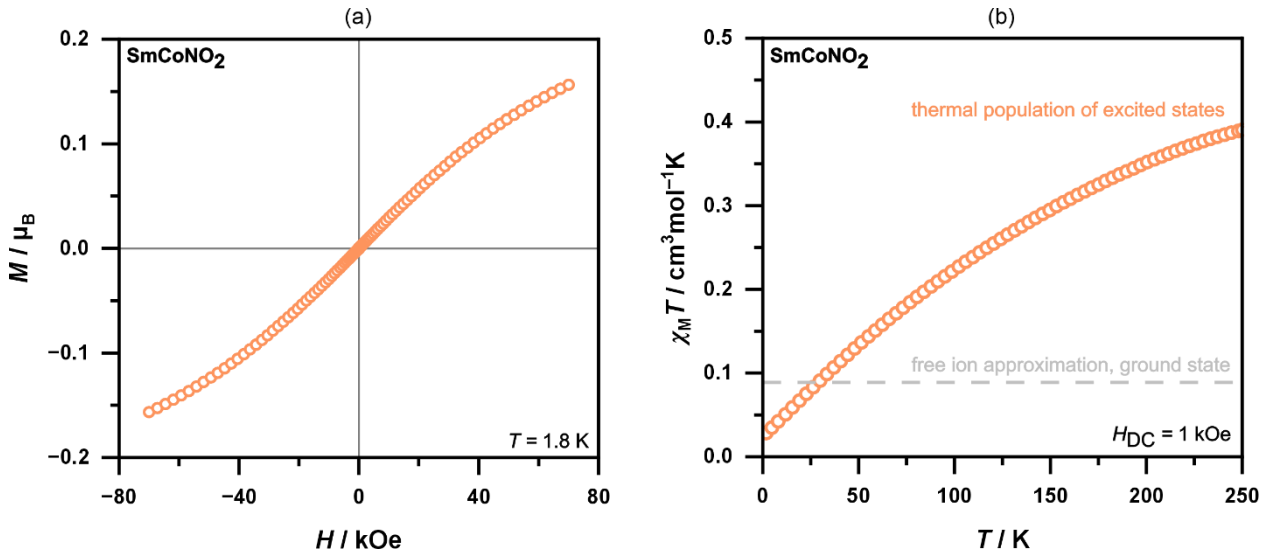

Fig. S16 Direct-current (DC) magnetic characteristics of **$SmCoNO_2$**, including the magnetization versus magnetic field curve at 1.8 K (a) and the temperature dependence of the magnetic susceptibility–temperature product under H_{DC} = 1 kOe (b). In the (b) part, the level of the magnetic signal corresponding to the free-ion approximation (without taking into account the thermally populated excited states) is indicated.[S14]

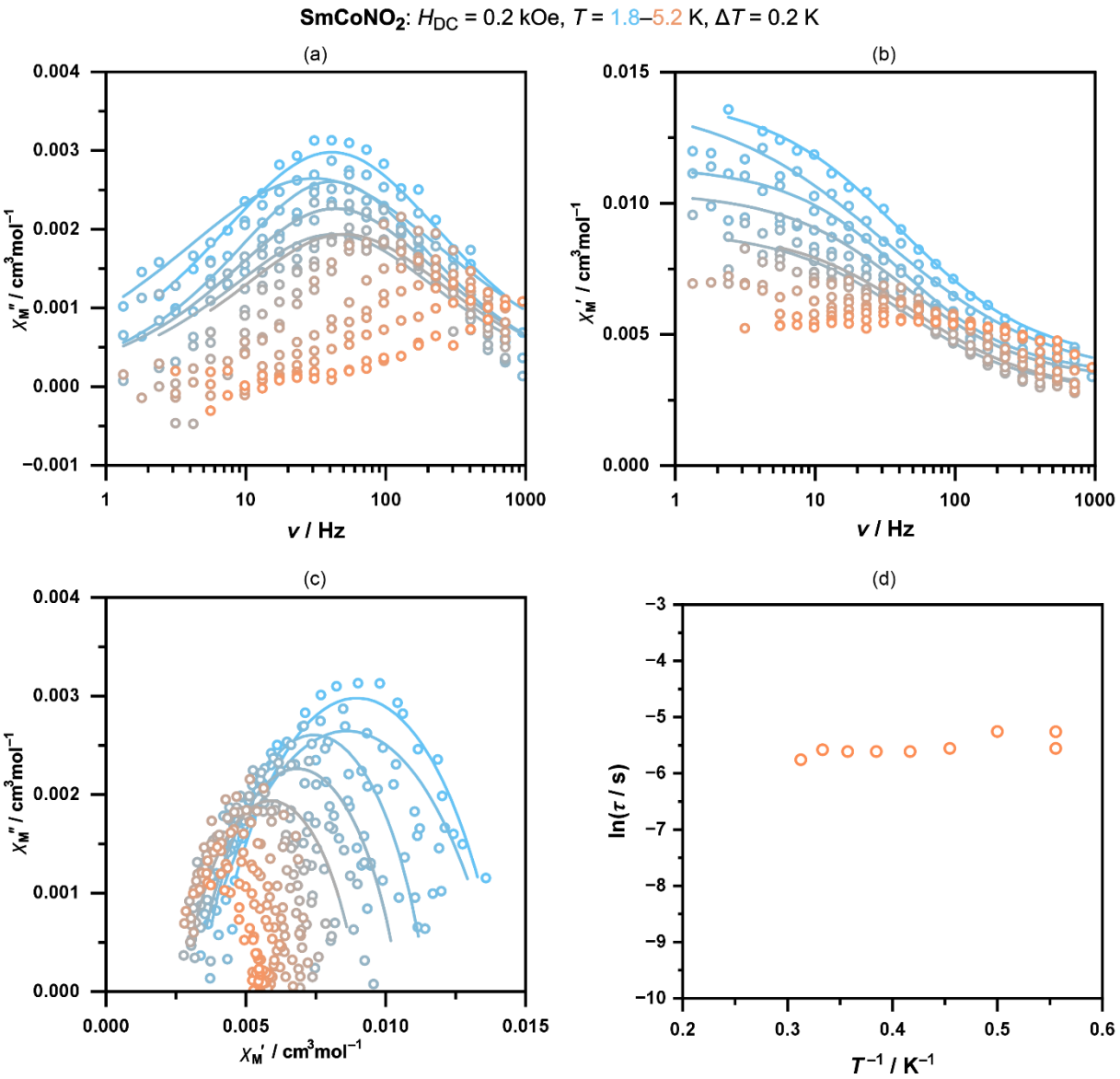

Fig. S17 Temperature-variable alternate-current (AC) magnetic characteristics for **$SmCoNO_2$** under H_{DC} = 0.2 kOe, including the frequency dependencies of the imaginary part of complex AC susceptibility (a), the frequency dependencies of the real part of complex AC susceptibility (b), the related Argand plots (c), and the temperature dependence of the resulting magnetic relaxation times (d). For the (a, b, c) parts, the best fits to the generalized Debye model of a single relaxation process, which were achievable for part of the gathered data, were shown as solid lines. In the (d) part, only experimental relaxation times are presented, as the fitting of this dependence to the combinations of magnetic relaxation processes was unsuccessful.

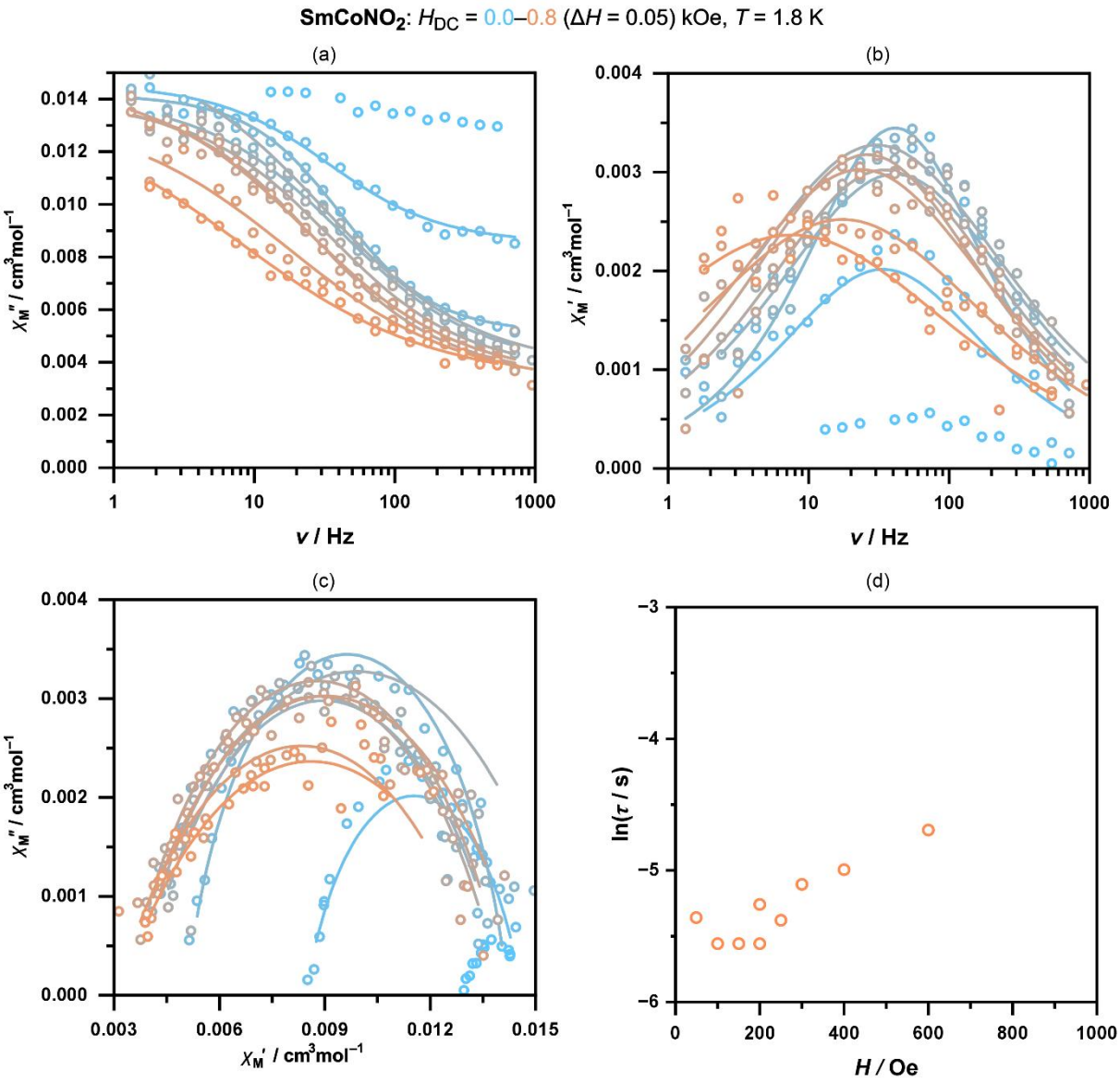

Fig. S18 DC-field-variable alternate-current (AC) magnetic characteristics for **$SmCoNO_2$** at T = 1.8 K, including the frequency dependencies of the imaginary part of complex AC susceptibility (a), the frequency dependencies of the real part of complex AC susceptibility (b), the related Argand plots (c), and the DC-field dependence of the resulting magnetic relaxation times (d). For the (a, b, c) parts, the best fits to the generalized Debye model of a single relaxation process, which were achievable for part of the gathered data, were shown as solid lines. In the (d) part, only experimental relaxation times are presented, as the fitting of this dependence to the combinations of magnetic relaxation processes was unsuccessful.

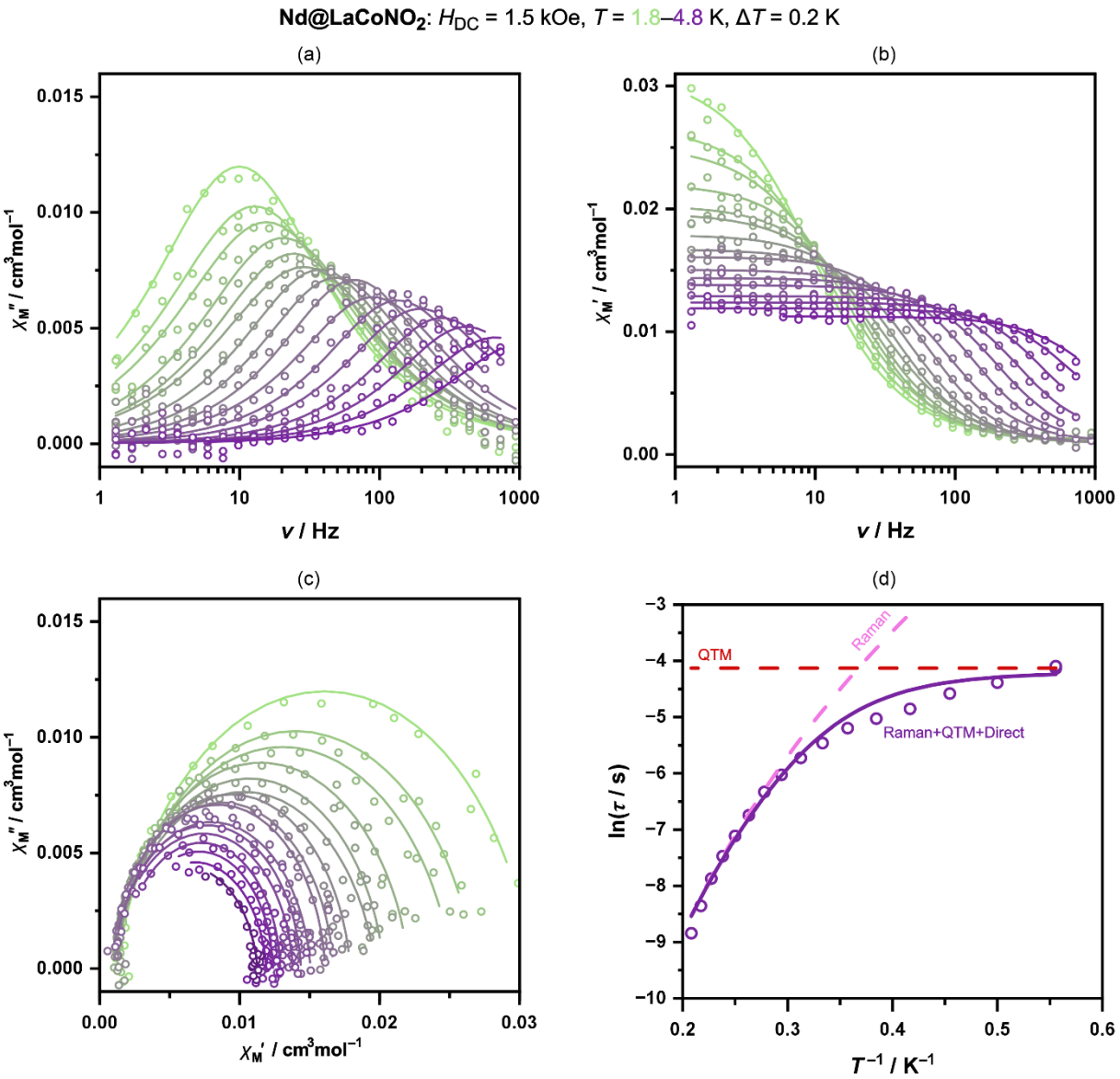

Fig. S19 Temperature-variable alternate-current (AC) magnetic characteristics for **Nd@LaCoNO$_2$** under H_{DC} = 1.5 kOe, including the frequency dependencies of the imaginary part of complex AC susceptibility (a), the frequency dependencies of the real part of complex AC susceptibility (b), the related Argand plots (c), and the temperature dependence of the resulting magnetic relaxation times (d). For the (a, b, c) parts, the best fits to the generalized Debye model of a single relaxation process were shown as solid lines. For the (d) part, a solid line represents the best-fit curve obtained using the combined contributions from QTM, Raman, and Direct processes, while dashed lines represent the separate contributions from the indicated processes. Note that the fit presented in the (d) part was performed as a simultaneous one with the related DC-field dependence of relaxation times and the additional *T*-dependence of relaxation times under the different DC field (see Fig. S20 and S21), which was realized using the relACs software.[S15]

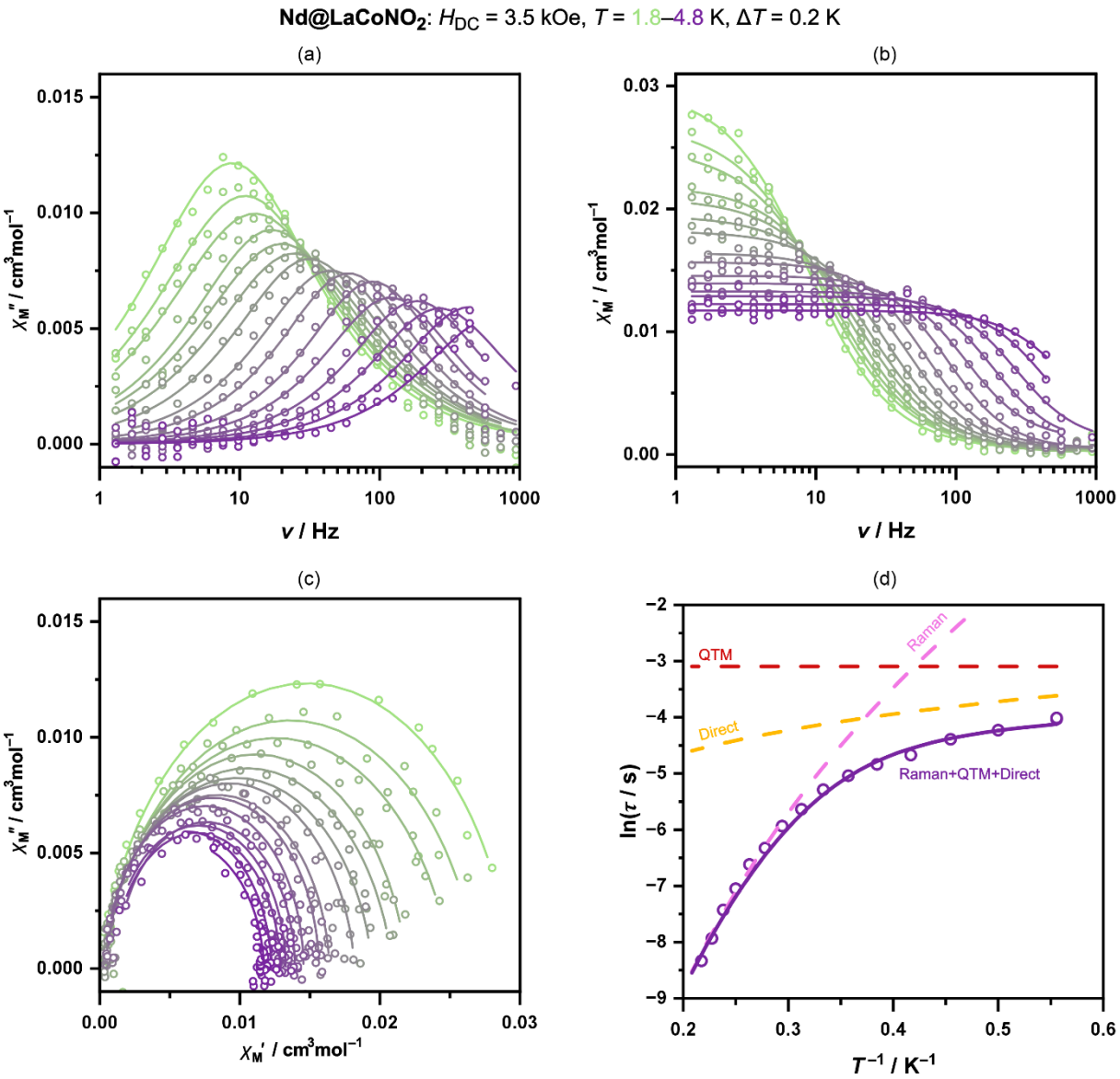

Fig. S20 Temperature-variable alternate-current (AC) magnetic characteristics for **Nd@LaCoNO$_2$** under H_{DC} = 3.5 kOe, including the frequency dependencies of the imaginary part of complex AC susceptibility (a), the frequency dependencies of the real part of complex AC susceptibility (b), the related Argand plots (c), and the temperature dependence of the resulting magnetic relaxation times (d). For the (a, b, c) parts, the best fits to the generalized Debye model of a single relaxation process were shown as solid lines. For the (d) part, a solid line represents the best-fit curve obtained using the combined contributions from QTM, Raman, and Direct processes, while dashed lines represent the separate contributions from the indicated processes. Note that the fit presented in the (d) part was performed as a simultaneous one with the related DC-field dependence of relaxation times and the additional *T*-dependence of relaxation times under the different DC field (see Fig. S19 and S21), which was realized using the relACs software.[S15]

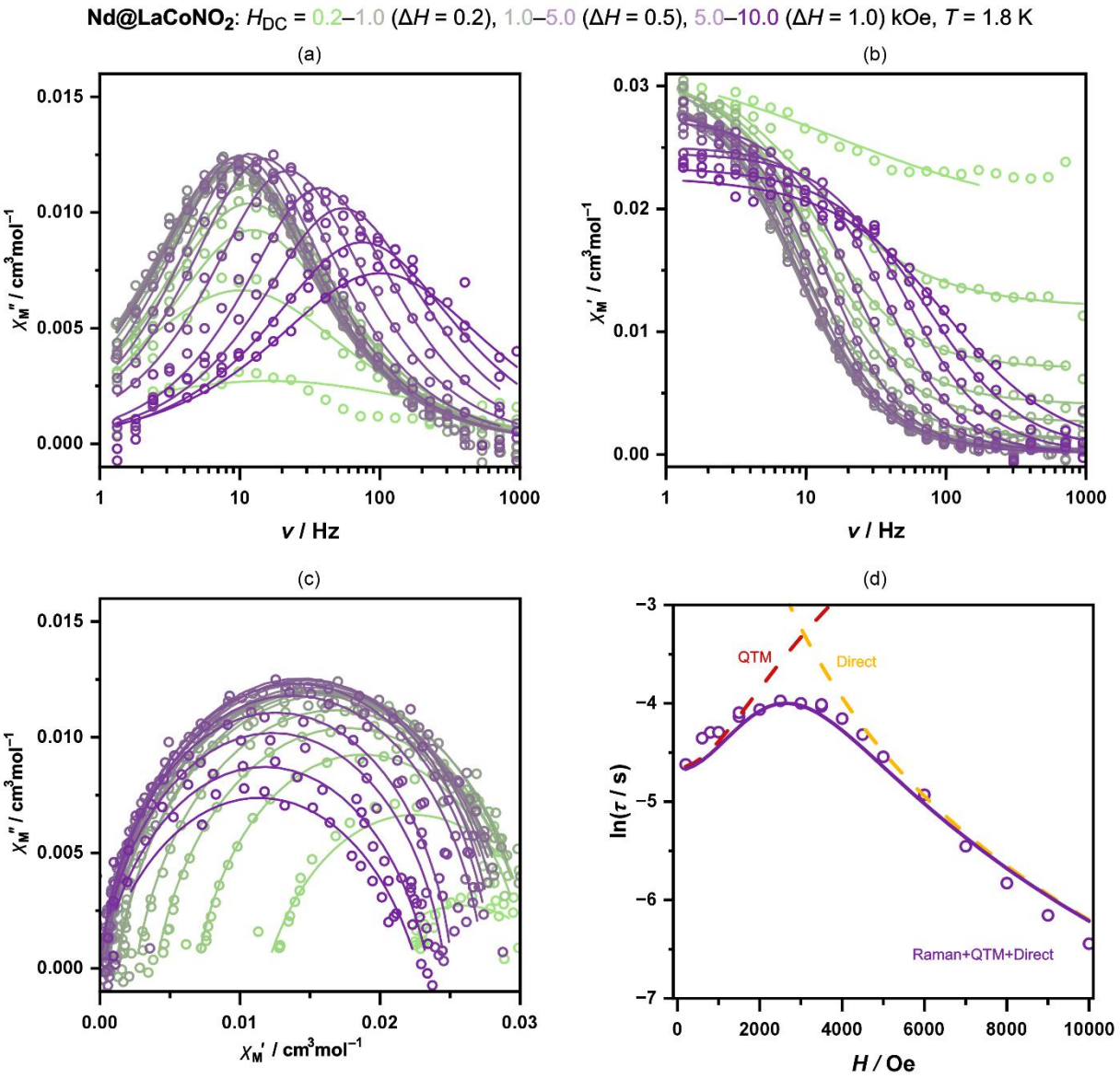

Fig. S21 DC-field-variable alternate-current (AC) magnetic characteristics for **Nd@LaCoNO$_2$** at T = 1.8 K, including the frequency dependencies of the imaginary part of complex AC susceptibility (a), the frequency dependencies of the real part of complex AC susceptibility (b), the related Argand plots (c), and the DC-field dependence of the resulting magnetic relaxation times (d). For the (a, b, c) parts, the best fits to the generalized Debye model of a single relaxation process were shown as solid lines. For the (d) part, a solid line represents the best-fit curve obtained using the combined contributions from QTM, Raman, and Direct processes, while dashed lines represent the separate contributions from the indicated processes. Note that the fit presented in the (d) part was performed as a simultaneous one with the related temperature dependences of relaxation times (see Fig. S19 and S20), which was realized using the relACs software.[S15]

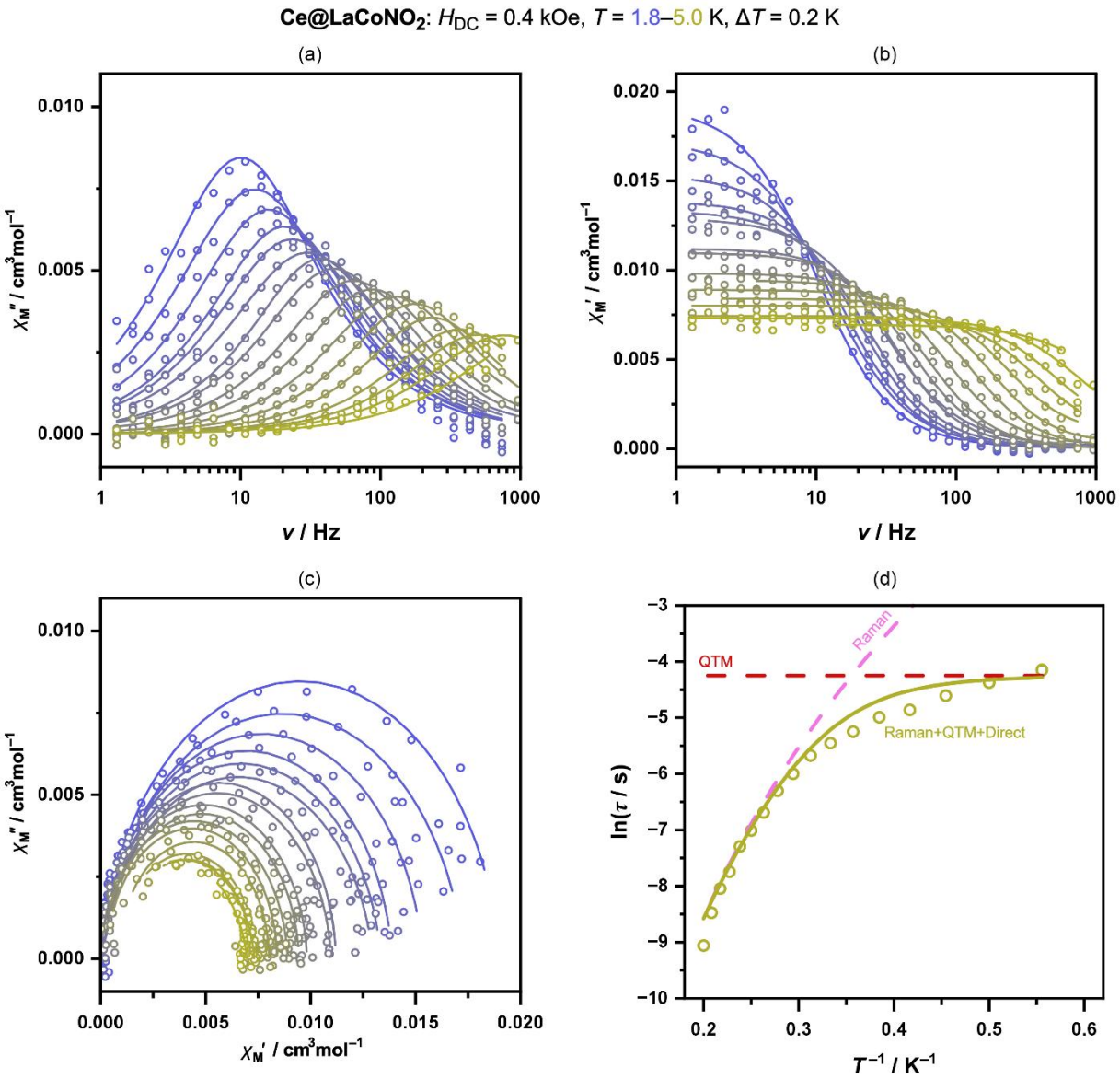

Fig. S22 Temperature-variable alternate-current (AC) magnetic characteristics for **Ce@LaCoNO$_2$** under H_{DC} = 0.4 kOe, including the frequency dependencies of the imaginary part of complex AC susceptibility (a), the frequency dependencies of the real part of complex AC susceptibility (b), the related Argand plots (c), and the temperature dependence of the resulting magnetic relaxation times (d). For the (a, b, c) parts, the best fits to the generalized Debye model of a single relaxation process were shown as solid lines. For the (d) part, a solid line represents the best-fit curve obtained using the combined contributions from QTM, Raman, and Direct processes, while dashed lines represent the separate contributions from the indicated processes. Note that the fit presented in the (d) part was performed as a simultaneous one with the related DC-field dependence of relaxation times and the additional *T*-dependence of relaxation times under the different DC field (see Fig. S23 and S24), which was realized using the relACs software.[S15]

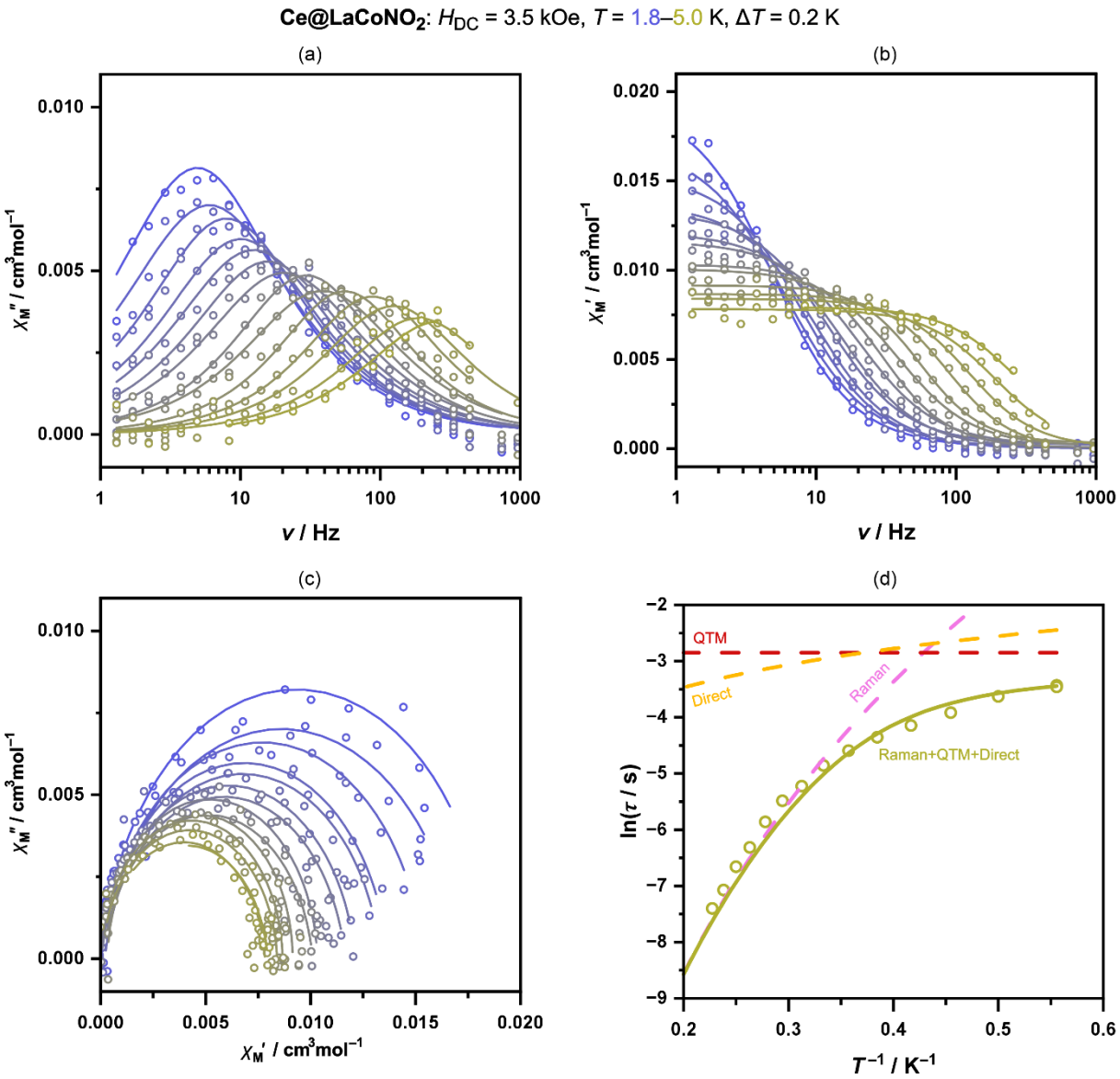

Fig. S23 Temperature-variable alternate-current (AC) magnetic characteristics for **Ce@LaCoNO$_2$** under H_{DC} = 3.5 kOe, including the frequency dependencies of the imaginary part of complex AC susceptibility (a), the frequency dependencies of the real part of complex AC susceptibility (b), the related Argand plots (c), and the temperature dependence of the resulting magnetic relaxation times (d). For the (a, b, c) parts, the best fits to the generalized Debye model of a single relaxation process were shown as solid lines. For the (d) part, a solid line represents the best-fit curve obtained using the combined contributions from QTM, Raman, and Direct processes, while dashed lines represent the separate contributions from the indicated processes. Note that the fit presented in the (d) part was performed as a simultaneous one with the related DC-field dependence of relaxation times and the additional *T*-dependence of relaxation times under the different DC field (see Fig. S22 and S24), which was realized using the relACs software.[S15]

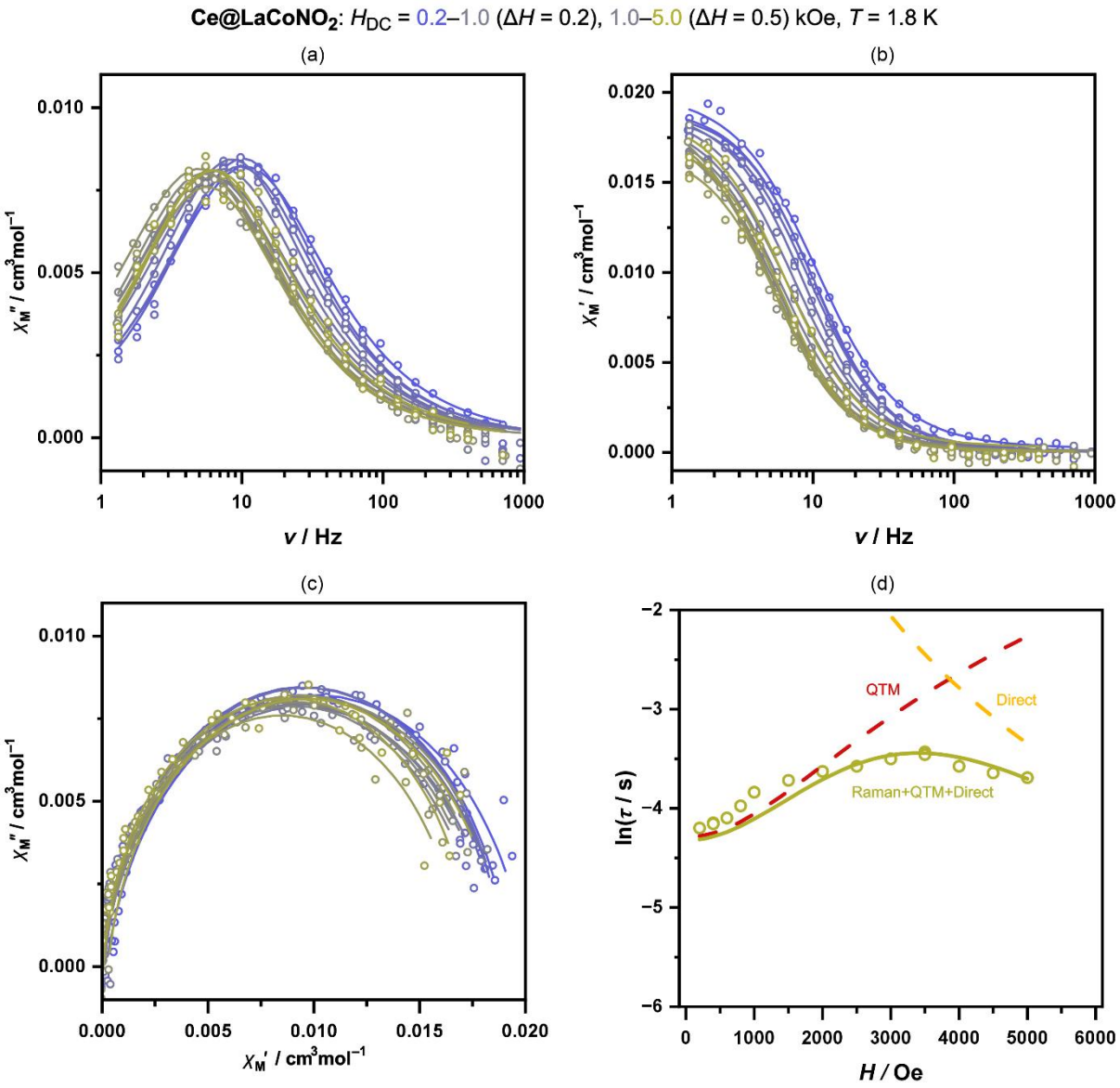

Fig. S24 DC-field-variable alternate-current (AC) magnetic characteristics for **Ce@LaCoNO$_2$** at T = 1.8 K, including the frequency dependencies of the imaginary part of complex AC susceptibility (a), the frequency dependencies of the real part of complex AC susceptibility (b), the related Argand plots (c), and the DC-field dependence of the resulting magnetic relaxation times (d). For the (a, b, c) parts, the best fits to the generalized Debye model of a single relaxation process were shown as solid lines. For the (d) part, a solid line represents the best-fit curve obtained using the combined contributions from QTM, Raman, and Direct processes, while dashed lines represent the separate contributions from the indicated processes. Note that the fit presented in the (d) part was performed as a simultaneous one with the related temperature dependences of relaxation times (see Fig. S22 and S23), which was realized using the relACs software.[S15]

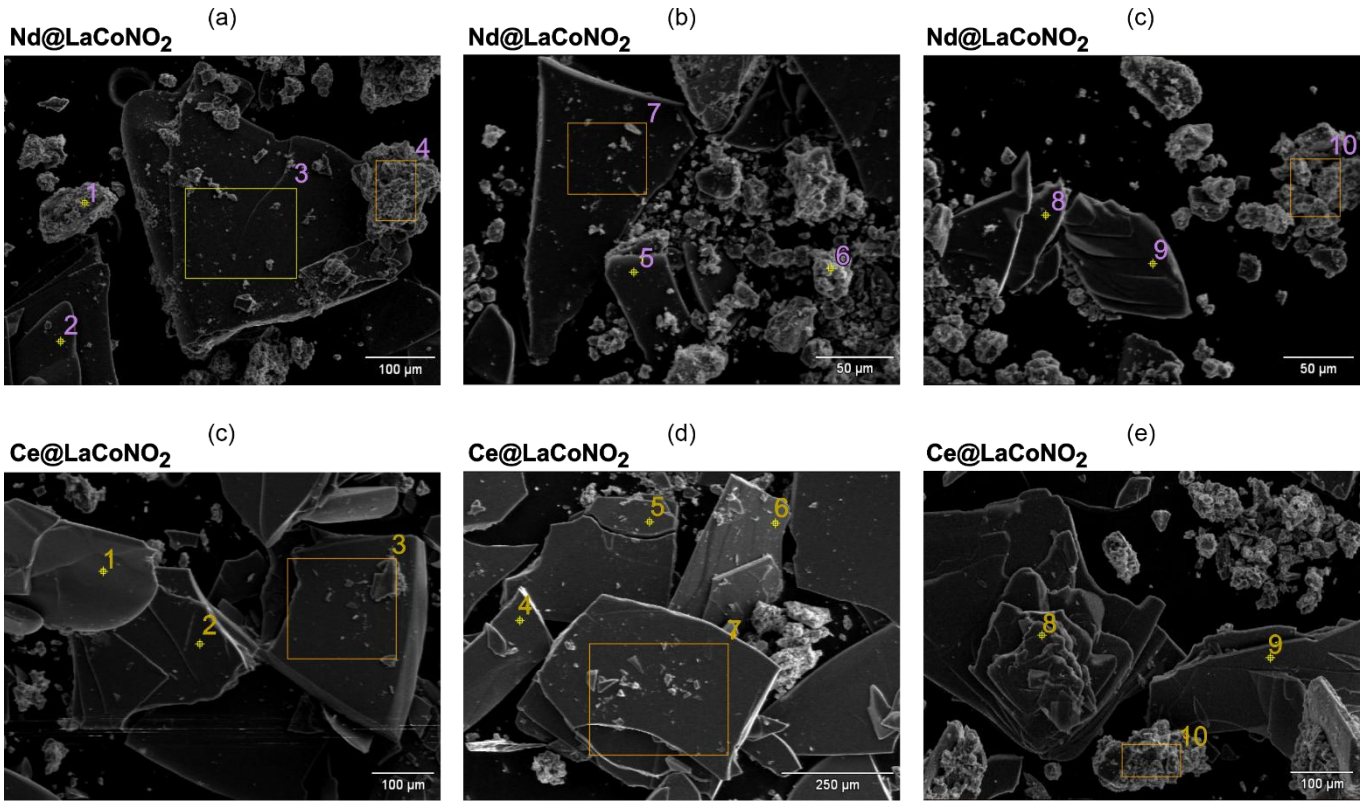

Fig. S25 SEM images taken for the selected points or areas of the crystals of **Nd@LaCoNO$_2$** (a, b, c) and **Ce@LaCoNO$_2$** (d, e, f), with the indicated probed points/areas (1–10) that were used for the EDX analysis of the metal composition. The related results are provided in Table S9.

Table S9 Results of SEM-EDX microanalyses performed for **Nd@LaCoNO$_2$** and **Ce@LaCoNO$_2$**, including the determined metal ratio for each probed point/area of the crystal (see Fig. S25) and the resulting average value of the metal ratios of the applied lanthanide ions. Note that the obtained La/Nd and La/Ce molar ratios were found to be slightly different than those determined by the ICP-MS method (see Experimental section). As this analysis should be considered as rather semi-quantitative and does not represent the metal ratios for the whole bulk samples, the analogous results from the ICP-MS measurements (which are considered to be more precise and represent the composition of the bulk samples) were used for the formula determination and the analysis of magnetic data. The good correlation between the direct-current magnetic data and the results from the ICP-MS method confirms the validity of this approach.

Compound	**Element: atomic fraction / %**			**Metal ratio (calculated for the total number of 1 lanthanide center per the formula unit)**
Nd@LaNO$_2$	**La**	**Nd**	**Co**	**La/Nd**
1	35.4(18)	6.4(11)	58.3(31)	0.847/0.153
2	39.0(12)	3.9(18)	58.5(33)	0.909/0.091
3	41.6(22)	5.8(14)	53(6)	0.878/0.122
4	42.7(21)	5.1(13)	52.3(34)	0.893/0.107
5	39.7(13)	5.4(14)	55(6)	0.880/0.120
6	41.1(22)	9.2(14)	50(6)	0.827/0.183
7	38.5(13)	7.3(13)	54.2(34)	0.841/0.159
8	34.5(20)	3.4(21)	52(5)	0.910/0.090
9	32.3(36)	8.1(22)	60(6)	0.800/0.200
10	experimental error (lack of reliable data)			–
Average:				**0.86(1)/0.14(1)**
Ce@LaNO$_2$	**La**	**Ce**	**Co**	**La/Ce**
1	36.4(26)	4.9(18)	58.7(26)	0.881/0.119
2	38.7(28)	6.7(20)	55(4)	0.852/0.148
3	36.5(15)	7.7(17)	55.8(29)	0.826/0.164
4	experimental error (lack of reliable data)			–
5	37.5(18)	6.2(12)	56.4(26)	0.858/0.142
6	39.8(20)	5.4(14)	54.9(29)	0.881/0.119
7	38.1(21)	6.0(15)	56(3)	0.864/0.136
8	37.2(21)	5.8(15)	57.0(21)	0.865/0.135
9	41.3(11)	7.1(13)	52(3)	0.853/0.147
10	37.5(24)	8.4(17)	54(4)	0.817/0.183
Average:				**0.86(1)/0.14(1)**

Table S10 Best-fit parameters of the field- and temperature-dependencies of magnetic relaxation times of **$NdCoNO_2$**, **$Nd@LaCoNO_2$**, **$CeCoNO_2$**, and **$Ce@LaCoNO_2$** to the equation S1, which was shown below the table. The related best-fit curves are presented in the figures gathered above.

Parameter	$NdCoNO_2$	$Nd@LaCoNO_2$	$CeCoNO_2$	$Ce@LaCoNO_2$
C_{Raman} / $s^{-1}K^{-n}$	5.2(13)	0.027(10)	3.5(5)	0.030(13)
n	4.51(19)	7.74(27)	4.87(10)	7.5(3)
B_1 / s^{-1}	234(16)	105(10)	159(7)	74(6)
B_2 / $10^{-8}Oe^{-2}$	3.0(7)	30(9)	3.7(5)	27(7)
A_{Direct} / $10^{-8}K^{-1}Oe^{-m}s^{-1}$	–	3.8(4)	–	0.72(23)
m	–	2.465(8)	–	2.525(22)

Comment to Table S10, related to the measurements and the fitting of AC magnetic data in $NdCoNO_2$, $Nd@LaCoNO_2$, $CeCoNO_2$, and $Ce@LaCoNO_2$

The 1.5 kOe DC field was used for *T*-dependent AC susceptibility studies for **$NdCoNO_2$** and its magnetically diluted analog of **$Nd@LaCoNO_2$**. We selected this field based on the analysis of the field-dependent AC studies for the primarily investigated **$NdCoNO_2$** (Fig. S13). For this compound, there is a continuous increase in magnetic relaxation time upon the increase of DC magnetic field due to the QTM quenching, without the appearance of the Direct process in the studied 0–5 kOe range. Therefore, there is no specific optimal DC field in the context of the slowest relaxation time. It could have been postulated to be at the highest 5 kOe field, for which the relaxation time is indeed the slowest. However, for the high fields from the indicated range, the key maxima of the χ_M"(ν) dependencies are not clearly shaped, as the related peaks are very broad and weak in comparison to those for smaller DC fields. Therefore, we took into account the strength of the χ_M" signal and the distinct shape of the χ_M"(ν) maxima. In this context, the highest χ_M" signal with the clear (i.e., relatively sharp) χ_M"(ν) peak was found for the 1.5 kOe DC field (Fig. S13a). Thus, this one was selected as an optimal DC field for the *T*-dependent AC studies (Fig. 3a and S12).

After completing the AC measurements for undiluted **$NdCoNO_2$**, we moved to the studies of its magnetic diluted sample of **$Nd@LaCoNO_2$**. We also started with the analysis of the field-dependent AC studies (Fig. S21). For this case, we found the appearance of both the QTM effect (dominating at low *H*-fields) and the Direct process (dominating at high *H*-fields). As a result, from the perspective of the slowest relaxation time, there is an optimal DC field of ca. 3.5 kOe, for which we performed the full set of *T*-dependent AC studies (Fig. S20). However, in addition to these results, we also performed the full set of *T*-dependent AC studies for the field of 1.5 kOe to show a better comparison with the undiluted sample (for which this field was an optimal one, as stated above; Fig. 3b and S19). For the final fitting of the contributions from all relaxation processes, we three mentioned datasets (the *H*-dependent AC studies at 1.8 K, and the *T*-dependent AC studies for the two indicated fields).

The analogous methodology was employed for **$CeCoNO_2$** and its magnetically diluted analog of **$Ce@LaCoNO_2$**, as the AC dependencies were quite analogous. The optimal DC field was deduced to be 0.4 kOe for **$CeCoNO_2$**, mainly based on the highest χ_M" signal with the clear χ_M"(ν) peak, and for this DC field, the *T*-dependent data were collected (Fig. 2c, S14, and S15). The optimal DC field was determined to be 3.5 kOe for **$Ce@LaCoNO_2$**, for which the relaxation time is the slowest, and for this field, the *T*-dependent data were collected; however, for the sake of comparison, the *T*-variable data for the 0.4 kOe of the DC field were also gathered and analyzed (Fig. 3d and S22–S24).

Concerning the fitting of the resulting relaxation times (obtained using a generalized Debye model from the described sets of the AC characteristics), the field- and temperature-variation of magnetic relaxation times in the reported family of compounds can be described by the following equation S1:

$$\tau^{-1} = C_{Raman}T^n + \frac{B_1}{1+B_2H^2} + A_{Direct}TH^m \qquad \text{(S1)}$$

where the first term represents the Raman relaxation (parameters of C_{Raman} and n), the second one corresponds to the quantum tunneling of magnetization (QTM) (parameters of B_1 and B_2), while the third one shows the Direct process (with parameters of A_{Direct} and m).[S3,S16,S17] Note that the Direct process was not necessary to obtain the high-quality fits for the undiluted samples of **$NdCoNO_2$** and **$CeCoNO_2$** (only Raman and QTM processes were employed).

Details of the *ab initio* calculations

The *ab initio* calculations were carried out for the compounds with the detected pronounced slow magnetic relaxation effects (i.e., **$CeCoNO_2$** and **$NdCoNO_2$**), using the crystal structures of the related compounds taken from the results of the respective single-crystal XRD experiments. The molecular fragments, which were selected for the calculations, consisted of the lanthanide(III) centers (Ce(III) or Nd(III), depending on the compound) and all of the molecules coordinated to each of them (two 4,4'-bpdo ligands, three cobalt(III) complexes, and four water molecules, Fig. S26a). The static structural disorder related to the two positions of the NO_2^- ligand within the cobalt(III) complex was considered, but its effect on the final results was found to be negligible. The calculations consisted of three steps. Firstly, the positions of the hydrogen atoms were optimized, as it was found to be a more reliable method for the determination of their exact positions than their direct consideration from the SC-XRD structural model. Then, a state average complete active space self-consistent field (SA-CASSCF) *ab initio* calculations were performed. Finally, the magnetic properties of the investigated systems were simulated and compared with the experiments.

The optimization of the hydrogen atoms' positions was carried out in the ORCA 6.0.1 quantum chemistry software package as a constrained optimization with all non-hydrogen atoms locked at their positions determined by the SC-XRD method.[S18–S22] To ensure reliable results for the hydrogen atoms in water molecules directly coordinated to the lanthanide centers, the molecular system for this geometry optimization was expanded to include a cyanido ligand and four water molecules that were connected to them through hydrogen bonds (Fig. S26b). Moreover, to aid in the wavefunction convergence, the Ce or Nd atoms were replaced with La for the optimization. The calculations utilized the M06 meta-GGA functional and def2-SVP basis set with ORCA's default effective core potential (ECP) for the lanthanum, D4 long-range dispersion corrections, RIJCOSX approximations to reduce the computational costs, and conductor-like polarizable continuum solvent model (C-PCM) of a perfect conductor.[S23–S32] Such a combination of parameters was reported to be effective for the analogous cases of molecular systems that can be found in the literature.[S33]

The SA-CASSCF calculations were performed using OpenMolcas software.[S34] Scalar relativistic effects were taken into account by employing a two-component second-order Douglas-Kroll-Hess (DKH2) Hamiltonian together with relativistic atomic natural orbital basis sets of ANO-RCC type.[S35–S37] To save disk space for computations, Cholesky decomposition of ERI-s (electron repulsion integrals) was used with the $1.0 \cdot 10^{-8}$ threshold. The implemented basis functions were VTZP for the lanthanide(III) ions and VDZP for atoms directly coordinated to it, and VDZ for other atoms. A description of the basis set used and its contractions are presented in Table S11. In the CASSCF step, the active space was composed of seven 4f orbitals of Ce(III) or Nd(III) centers with 1 for Ce and 3 for Nd active electron(s), then 7 doublets for Ce and 35 quartets/112 doublets for Nd spin-adapted states arising from different possible electron distributions in 4f orbitals were evaluated. In the next step, all previously optimised spin-free states were mixed within the restricted active space state interaction (RASSI) submodule by spin-orbit coupling (SOC) within the atomic mean field (AMFI) approximation.[S38,S39]

The magnetic properties of the investigated system were evaluated with the SlothPy software package, based on the results given by the RASSI module of OpenMolcas.[S3] The theoretical magnetization over magnetic field and magnetic susceptibility and temperature product over temperature for compounds **$CeCoNO_2$** and **$NdCoNO_2$** are presented in Fig. S27. They exhibit good agreement with the experimental data. The energy splitting of the ground multiplet of the lanthanide centers with pseudo-*g*-tensor components and the composition of the Kramers doublets in the $|m_J\rangle$ basis for **$CeCoNO_2$** and **$NdCoNO_2$** are presented in Tables S12 and S13, respectively. Both compounds suffer from significant pseudo-*g*-tensor transversal components and high mixing of states, which is in line with them exhibiting only DC-field-induced slow magnetic relaxation (see Fig. 3 and the main article for details).

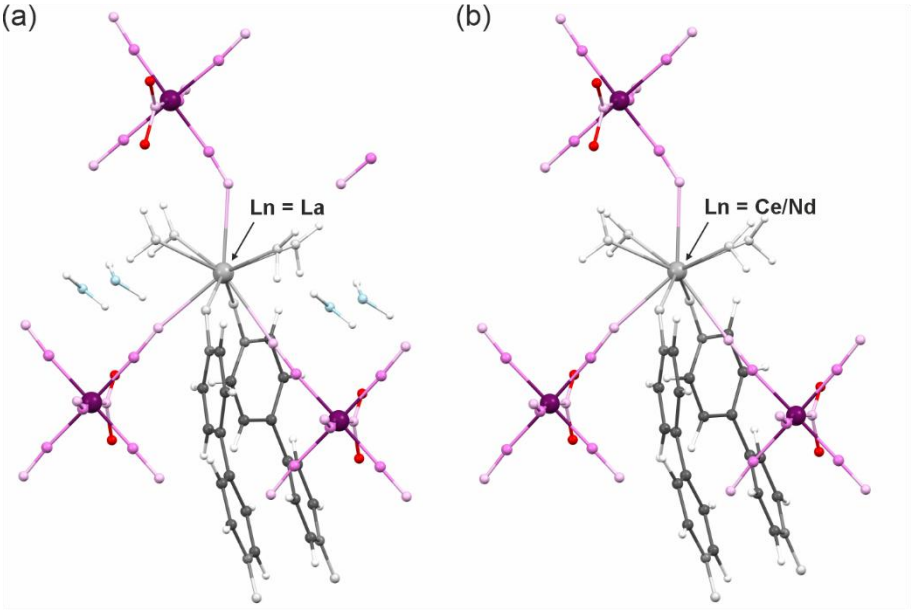

Fig. S26 The expanded molecular fragment of **$LnCoNO_2$** used for the optimization of the positions of H-atoms (a model with additional molecules H-bonded with crucial coordinated water molecules and with La(III) centers placed at the lanthanide position, see the text above for further details) (a) and the reduced molecular fragment used for subsequent SA-CASSCF calculations and the further simulation of the magnetic properties (b). The figure is based on the crystal structure of **$CeCoNO_2$**; however, the analogous procedure was also done for **$NdCoNO_2$**.

Table S11 Description and contractions of the basis set employed in the SA-CASSCF calculations for Ce(III) complexes in **$CeCoNO_2$** and Nd(III) complexes in **$NdCoNO_2$**.

Relativistic ANO basis sets — ANO-RCC	
Nd.ANO-RCC-VTZP	8S7P4D3F2G1H
Ce.ANO-RCC-VTZP	8S7P4D3F2G1H
Co.ANO-RCC-VDZ	5S4P2D
O.ANO-RCC-VDZP (coordinating oxygen)	3S2P1D
O.ANO-RCC-VDZ (non-coordinating oxygen)	3S2P
N.ANO-RCC-VDZP (coordinating nitrogen)	3S2P1D
N.ANO-RCC-VDZ (non-coordinating nitrogen)	3S2P
C.ANO-RCC-VDZ	3S2P
H.ANO-RCC-VDZ	2S

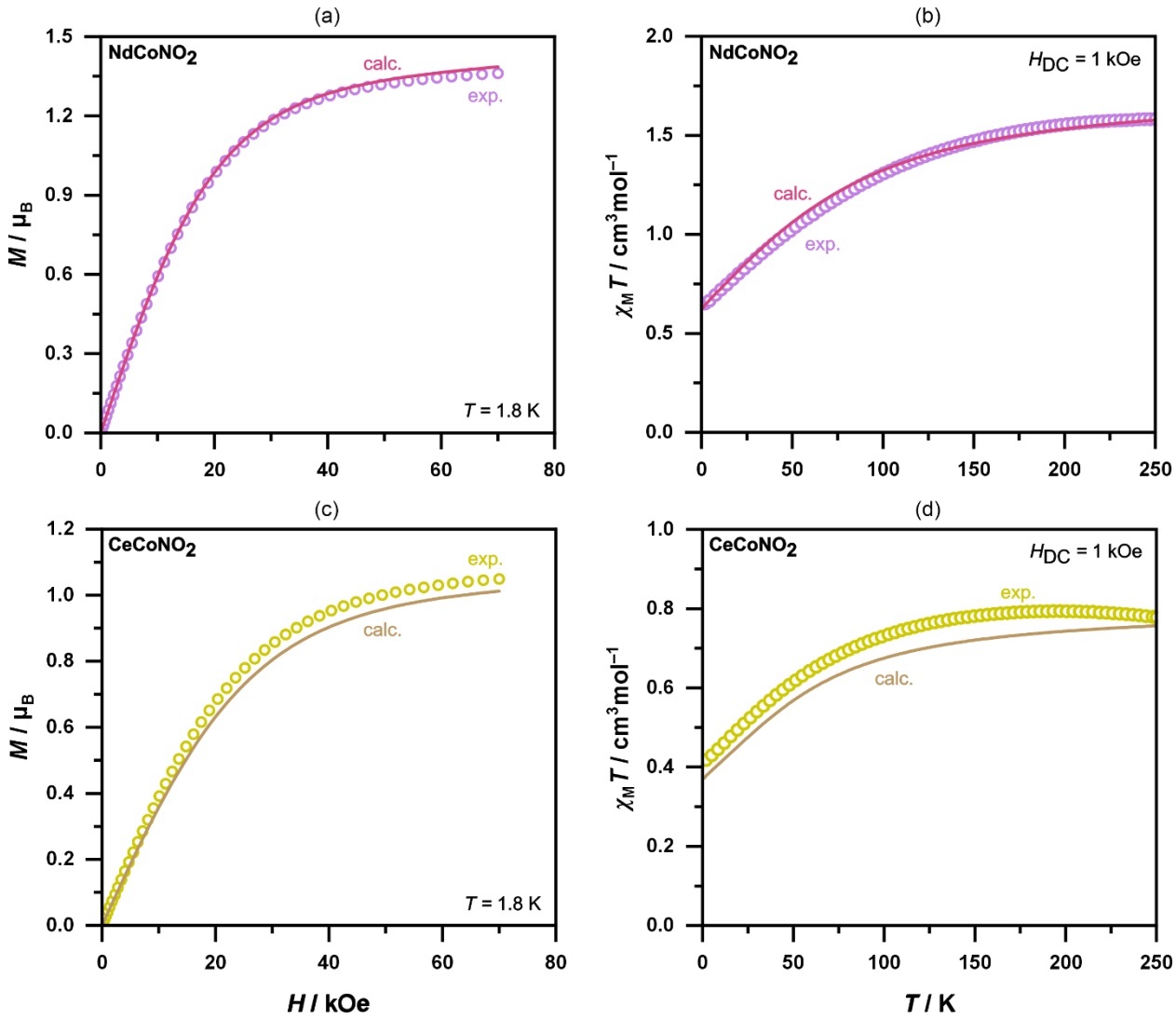

Fig. S27 Comparison of the *ab initio*-simulated (calc.) magnetization versus magnetic field curves (a, c) and the *ab initio*-simulated (calc.) temperature dependencies of the magnetic susceptibility–temperature product (b, d) of **$NdCoNO_2$** (a, b) and **$CeCoNO_2$** (c, d) with the respective experimental data (exp.).

Table S12 The results of the *ab initio* calculations for **$CeCoNO_2$**, including the energy splitting of the three SOC doublets of the ground $^2F_{5/2}$ multiplet, their main magnetic axes (pseudo-*g*-tensor components), and the composition of Kramers' doublets presented in the $|J = 5/2, m_J\rangle$ basis.

Energy and pseudo-*g*-tensor components (g_x, g_y, g_z) of three ground Kramers doublets				
Doublet no.	Energy / cm^{-1}	Pseudo-*g*-tensor components		
		g_x	g_y	g_z
1.	0.000	1.2173	1.8441	2.6390
2.	81.790	0.6741	0.7907	3.6220
3.	186.058	0.2128	0.8382	3.1983

Composition of the ground Kramers' doublets in the $\|m_J\rangle$ basis on the quantization axes within $J = 5/2$ manifold		
1st doublet	2nd doublet	3rd doublet
3.9% $\|-5/2\rangle$ 20.0% $\|-3/2\rangle$ 1.0% $\|-1/2\rangle$ 1.3% $\|+1/2\rangle$ 2.2% $\|+3/2\rangle$ 71.7% $\|+5/2\rangle$	4.5% $\|-5/2\rangle$ 11.5% $\|-3/2\rangle$ 49.7% $\|-1/2\rangle$ 27.1% $\|+1/2\rangle$ 3.3% $\|+3/2\rangle$ 3.9% $\|+5/2\rangle$	15.5% $\|-5/2\rangle$ 1.0% $\|-3/2\rangle$ 17.2% $\|-1/2\rangle$ 3.8% $\|+1/2\rangle$ 62.1% $\|+3/2\rangle$ 0.4% $\|+5/2\rangle$

Table S13 The results of the *ab initio* calculations for **$NdCoNO_2$**, including the energy splitting of the three SOC doublets of the ground $^4I_{9/2}$ multiplet, their main magnetic axes (pseudo-*g*-tensor components), and the composition of Kramers' doublets presented in the $|J = 9/2, m_J\rangle$ basis.

Energy and pseudo-*g*-tensor components (g_x, g_y, g_z) of five ground Kramers doublets				
Doublet no.	Energy / cm^{-1}	Pseudo-*g*-tensor components		
		g_x	g_y	g_z
1.	0.000	1.9350	2.2406	3.3607
2.	77.773	1.2344	1.6847	3.0914
3.	124.689	0.0411	1.4411	4.4044
4.	234.043	0.4227	1.1822	3.3400
5.	259.812	0.5091	1.6706	2.9610
Composition of the ground Kramers' doublets in the $\|m_J\rangle$ basis on the quantization axes within $J = 9/2$ manifold				
1^{st} doublet	2^{nd} doublet	3^{rd} doublet	4^{th} doublet	5^{th} doublet
3.6% |–9/2⟩	2.4% |–9/2⟩	11.3% |–9/2⟩	6.4% |–9/2⟩	11.2% |–9/2⟩
2.1% |–7/2⟩	13.0% |–7/2⟩	3.3% |–7/2⟩	15.1% |–7/2⟩	10.8% |–7/2⟩
1.4% |–5/2⟩	4.4% |–5/2⟩	38.2% |–5/2⟩	3.4% |–5/2⟩	10.7% |–5/2⟩
1.4% |–3/2⟩	7.3% |–3/2⟩	1.1% |–3/2⟩	10.4% |–3/2⟩	3.4% |–3/2⟩
17.5% |–1/2⟩	12.5% |–1/2⟩	1.2% |–1/2⟩	16.9% |–1/2⟩	6.8% |–1/2⟩
2.3% |+1/2⟩	9.8% |+1/2⟩	0.7% |+1/2⟩	2.4% |+1/2⟩	30.0% |+1/2⟩
15.0% |+3/2⟩	33.0% |+3/2⟩	3.7% |+3/2⟩	19.0% |+3/2⟩	5.8% |+3/2⟩
18.2% |+5/2⟩	1.7% |+5/2⟩	17.9% |+5/2⟩	3.3% |+5/2⟩	0.7% |+5/2⟩
0.6% |+7/2⟩	13.2% |+7/2⟩	17.6% |+7/2⟩	11.3% |+7/2⟩	12.9% |+7/2⟩
37.8% |+9/2⟩	2.7% |+9/2⟩	5.1% |+9/2⟩	11.9% |+9/2⟩	7.6% |+9/2⟩

Table S14 Calculated electric dipole moment vectors (*p*) for the lanthanide(III) complexes (see Fig. S28) in the **$LnCoNO_2$** series of compounds, compared with the experimental values of their relative SHG intensity (with respect to the KDP reference).

Compound	*p* / D			SHG / % KDP
	$p_x \parallel$ a	$p_y \parallel$ b	$p_z \parallel$ c	
$CeCoNO_2$	−0.22	−11.63	**−29.83**	94(2)
$LaCoNO_2$	−0.14	−12.89	**−28.97**	86(2)
$NdCoNO_2$	−0.16	−11.43	**−29.64**	75(2)
$PrCoNO_2$	−0.21	−11.02	**−29.43**	102(2)
$SmCoNO_2$	−0.27	−11.14	**−28.07**	84(2)

Comment to Table S14: The electric dipole moment vectors (***p***) of compounds **$CeCoNO_2$**, **$LaCoNO_2$**, **$NdCoNO_2$**, **$PrCoNO_2$**, and **$SmCoNO_2$** were calculated at the same level of theory as the geometry optimization (see the related discussion on Page S37), as single-point calculations at geometry taken directly from the crystal structure. The evaluation was done for the asymmetric unit duplicated with the mirror plane going through the lanthanide and cobalt atoms (Fig. S28). To achieve a chemically sensible molecular fragment, the disorder in the CN^-/NO_2^- position had to be removed. The results are presented in Table S14. Only the $\boldsymbol{p_z}$ component of the vector ***p***, lying along the crystallographic axis ***c***, is important, as others are cancelled out after applying the full crystal lattice symmetry.

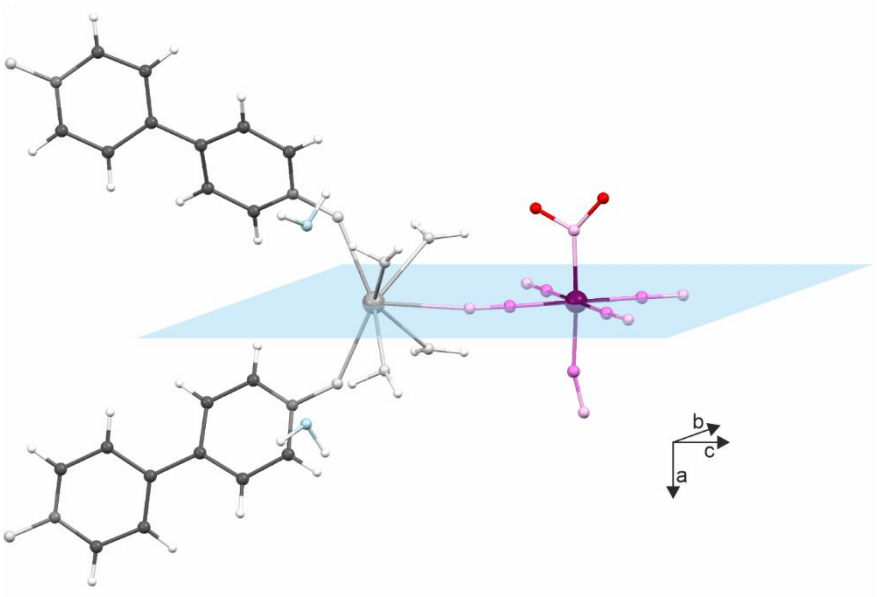

Fig. S28 The molecular fragment used for the evaluation of the electric dipole moment vector in relation to the main crystallographic axes of the compounds from the **$LnCoNO_2$** family (see Table S14 above). The light blue layer indicates the mirror plane used to duplicate the asymmetric unit. The figure is based on the crystal structure of **$CeCoNO_2$**, with the identical color code as shown in Fig. S1.

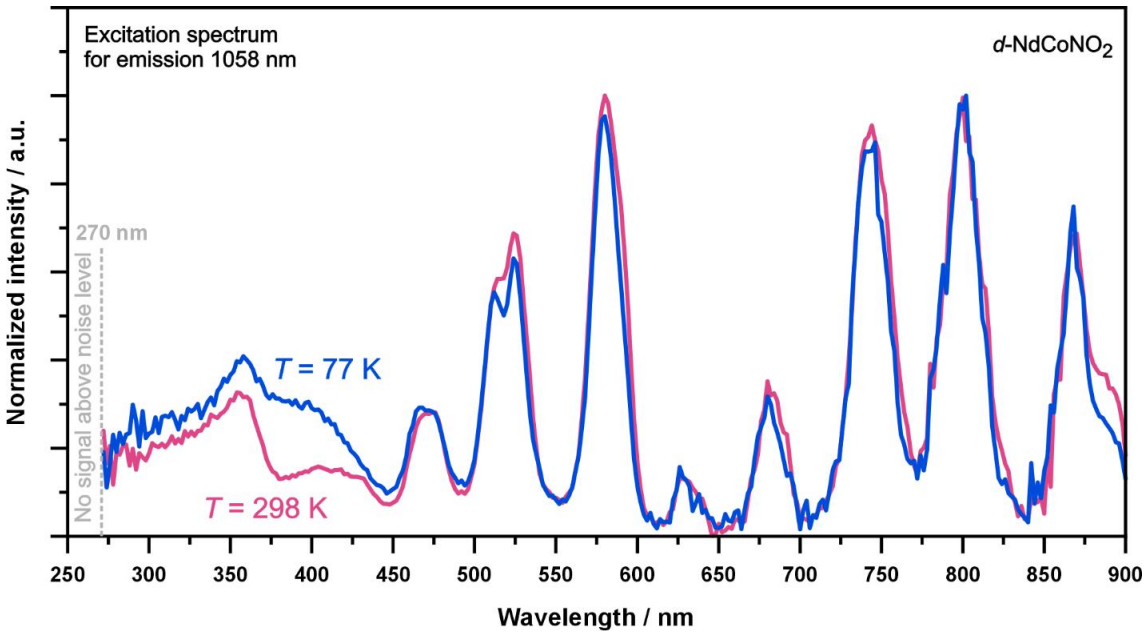

Fig. S29 Solid-state excitation spectra for the monitored indicated Nd(III)-centered emission of ***d*-NdCoNO$_2$** with the broadened spectral range of 270–900 nm at room temperature (298 K) and liquid nitrogen temperature (77 K). The experimental excitation wavelength limit related to the large noise level was indicated for clarity. For details regarding the role of these additional measurements (in comparison to the main data shown in Fig. 2c), see the comment on Page S49 below.

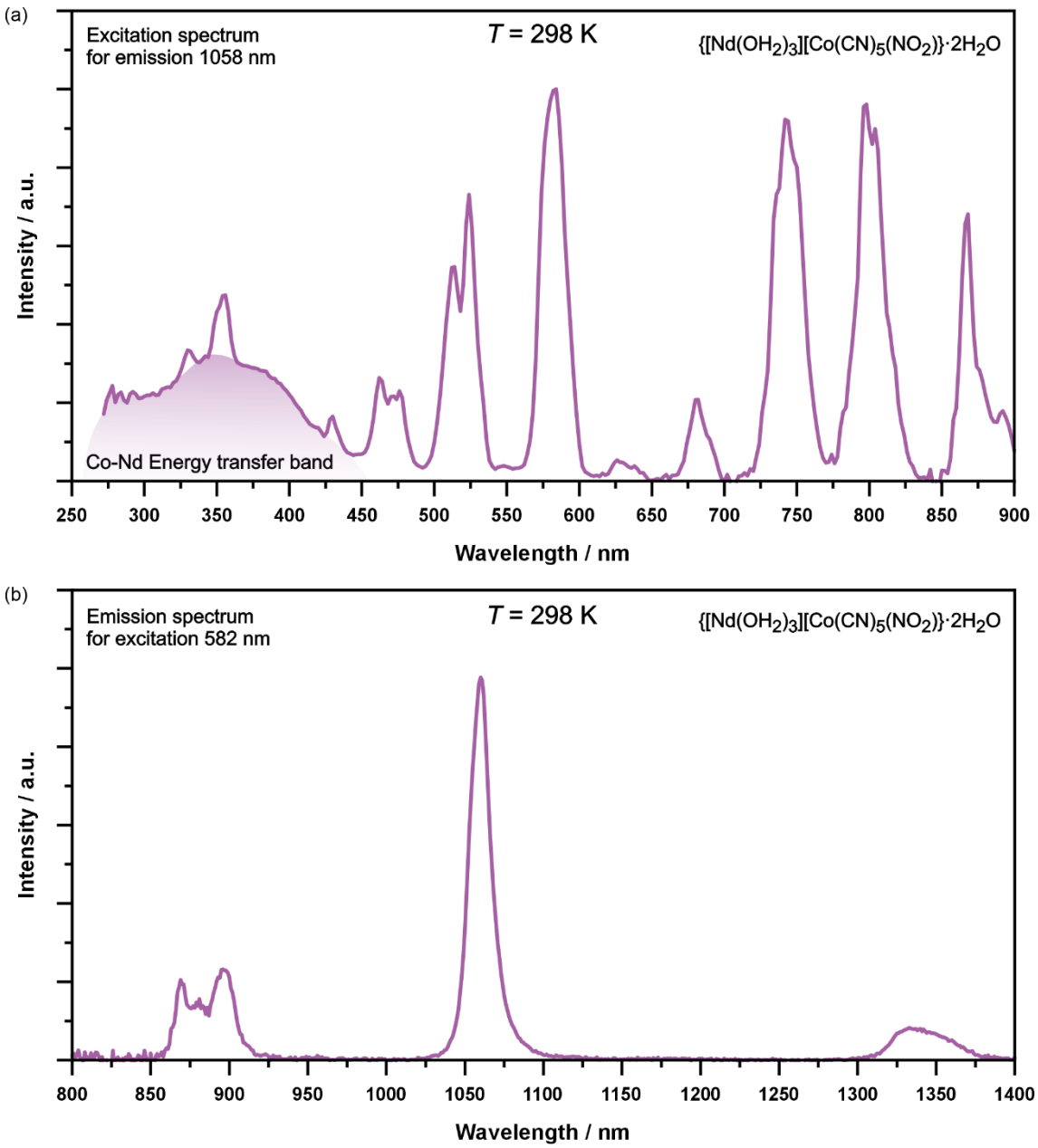

Fig. S30 Room-temperature solid-state excitation (a) and emission (b) spectra of the reference compound of $\{[Nd^{III}(OH_2)_3][Co^{III}(CN)_5(NO_2)]\}\cdot 2H_2O$. In (a) part, the excitation band representing the energy transfer from Co(III)-based metalloligand to Nd(III) centers was indicated by a colored area (labeled as Co-Nd Energy transfer band). For details regarding the role of these additional measurements of the reference compound, see the comment on Page S49 below.

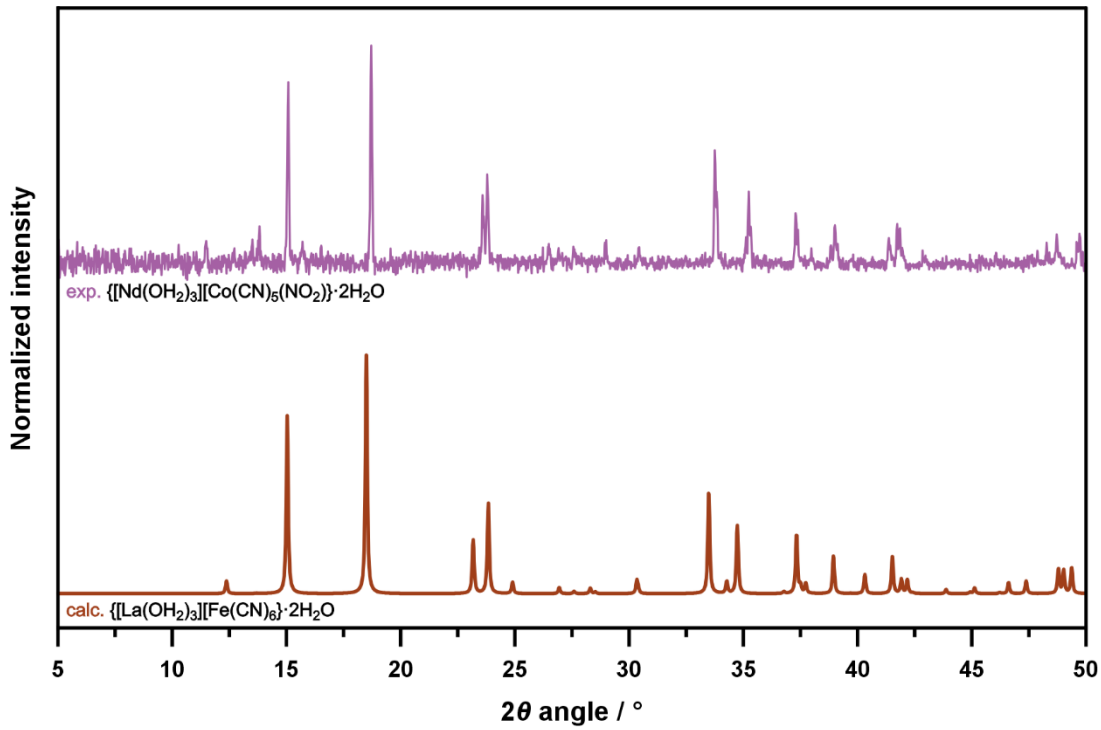

Fig. S31 Experimentally determined (exp.) powder X-ray diffraction (P-XRD) pattern of the reference compound of $\{[Nd^{III}(OH_2)_3][Co^{III}(CN)_5(NO_2)]\}\cdot 2H_2O$ compared with the calculated (calc.) pattern based on the structural model of the previously reported $\{[La^{III}(OH_2)_3][Fe^{III}(CN)_6]\}\cdot 2H_2O$ analog.[S40] For details regarding the role of this reference compound, see the comment on Page S49 below.

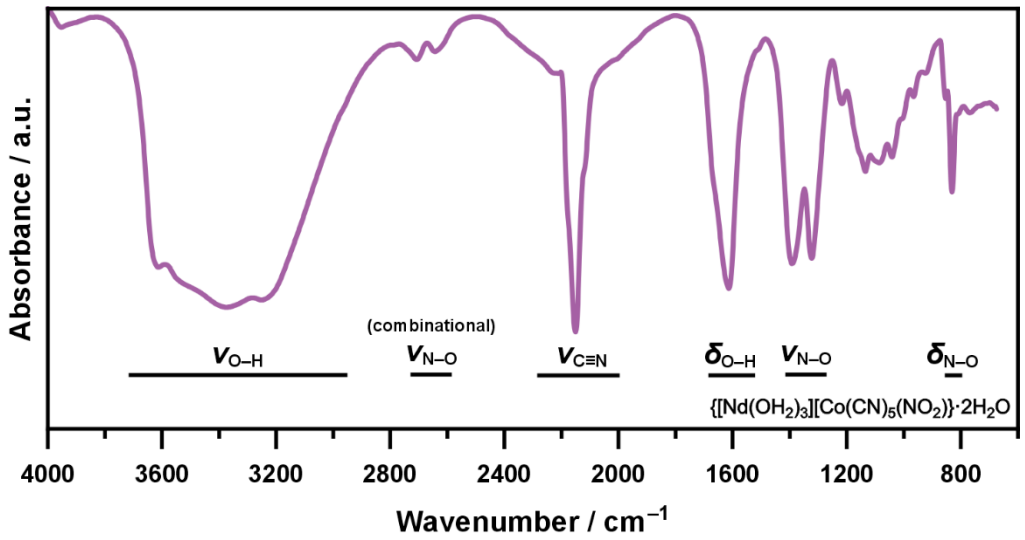

Fig. S32 Infrared (IR) absorption spectrum of the reference compound of $\{[Nd^{III}(OH_2)_3][Co^{III}(CN)_5(NO_2)]\}\cdot 2H_2O$ in the range of 4000–600 cm^{-1}. The interpretation of the main observed bands is presented in the graph. The assignment was based on the related compounds presented in this work (Fig. S3) and the referential ones, including the IR spectra for nitrito salts.[S3,S41] For details regarding the role of this reference compound, see the comment on Page S49 below.

Comment to Fig. S29–S32, i.e., on supporting studies aimed at the elucidation of the role of Co(III)-based metalloligands and 4,4'-bpdo ligands in the emission of Nd(III) complexes in $NdCoNO_2$

The excitation spectra for the monitored NIR emission of Nd(III) complexes in **$NdCoNO_2$** and its deuterated analog (Fig. 2c) suggested that, besides the direct f-f excitation, the non-negligible energy transfer from the Co(III) cyanido-nitrito complexes to the Nd(III) center can be postulated. This is depicted by the broad excitation band covering the 300–450 nm range. One can consider that the eventual additional excitation band, suggesting an alternative energy transfer pathway, e.g., involving 4,4'-bpdo, can be observed at higher energies. Such an excitation spectrum with the broadened wavelength range down to 270 nm could be gathered, as presented in Fig. S29. The resulting room- and low- (77 K) temperature excitation spectra (gathered for the deuterated form of the reported compound) were found to be very similar to those shown in Fig. 2c. More importantly, even at 77 K, there is no sign of the appearance of any novel excitation bands in the extended lower-wavelength range of 270–300 nm. Therefore, for the accessible wavelength range above 270 nm, it is rather possible to exclude the energy transfer from the 4,4'-bpdo organic ligand to the Nd(III) centers that could be induced by high UV energy.

Further considering the role of 4,4'-bpdo, we also checked that there is no emission in the visible range under any of the accessible, reliable UV range excitation. In such a case, one can postulate that the Co(III)-based metalloligand transfers the absorbed energy towards Nd(III) centers, but this energy transfer is only partial as the UV absorption of the metalloligand is expected to be relatively large while the resulting excitation band is much weaker than those related to the direct f-f excitation. Simultaneously, the 4,4'-bpdo ligand emission (sometimes observed in the blue-to-green region of the spectrum)[S42,S43] is quenched through non-radiative relaxation, and its eventual involvement in the ligand-to-metal energy transfer occurs with negligible efficiency.

To further confirm the assignment of a broad excitation band covering the 270–450 nm range to $[Co^{III}(CN)_5(NO_2)]^{3-}$ ions, not 4,4'-bpdo ligands, we synthesized the reference compound of a three-dimensional coordination polymer consisting exclusively of Nd^{III} and $[Co^{III}(CN)_5(NO_2)]^{3-}$ ions, and water molecules (i.e., without organic ligands, see Experimental section for details). The resulting $\{[Nd^{III}(OH_2)_3][Co^{III}(CN)_5(NO_2)]\}\cdot 2H_2O$ reference compound was proven, by the P-XRD pattern (Fig. S31), to be isostructural with the previously published $\{[La^{III}(OH_2)_3][Fe^{III}(CN)_6]\}\cdot 2H_2O$ analog.[S40] The presence of all expected molecular components in the reference compound was also confirmed by the IR spectroscopy (Fig. S32). We performed the PL studies for this reference compound, finding a very similar shape of the excitation spectrum when compared with the reported compound of **$NdCoNO_2$** (Fig. S30 and 2c). In particular, the key excitation band below 450 nm was found with a similar shape. Thus, it can be undoubtedly assigned to the $[Co^{III}(CN)_5(NO_2)]^{3-}$ metalloligands due to the lack of other molecular components that may reveal the broadband excitation in the reference compound. Therefore, for the reported compound of **$NdCoNO_2$**, it can be stated that only the mentioned Co(III) complex reveals the energy transfer to Nd(III) centers, and the eventual contribution from 4,4'-bpdo ligands is negligibly small.

Interestingly, the energy transfer pathway from Co(III)-based metalloligands to the Nd(III) centers in the reference compound seems to be better than in the reported one (compare Fig. S29 and S30), as is visible in the higher intensity of the related excitation band in comparison to the direct f-f excitation. This observation can be rationalized by the denser distribution of the Co(III) complexes and the higher number of their direct coordination to the Nd(III) centers in the 3-D framework in comparison to the reported 2-D coordination polymer of **$NdCoNO_2$**.

References to the Supporting Information

S1 R. Barca, J. Ellis, M.-S. Tsao and W. K. Willmarth, *Inorg. Chem.,* 1967, **6**, 243.

S2 T. Flor and J. Casabó, *Synth. React. Inorg. Met. Org. Chem.,* 1986, **16**, 795.

S3 M. Zychowicz, H. Dzielak, J. Rzepiela and S. Chorazy, *Inorg. Chem*., 2024, **63**, 19213.

S4 G. M. Sequeira, W. Y. Tan and E. G. Moore, *Dalton Trans*., 2015, **44**, 13378.

S5 G. M. Sheldrick, *Acta Crystallogr. A,* 2015, **71**, 3.

S6 G. M. Sheldrick, *Acta Crystallogr. C,* 2015, **71**, 3.

S7 L. J. Farrugia, *J. Appl. Cryst.,* 2012, **45**, 849.

S8 C. F. Macrae, I. Sovago, S. J. Cottrell, P. T. A. Galek, P. McCabe, E. Pidcock, M. Platings, G. P. Shields, J. S. Stevens, M. Towler and P. A. Wood, *J. Appl. Cryst.,* 2020, **53**, 226.

S9 R. Jankowski, J. J. Zakrzewski, M. Zychowicz, J. Wang, Y. Oki, S. Ohkoshi, S. Chorazy and B. Sieklucka, *J. Mater. Chem. C,* 2021, **9**, 10705.

S10 M. Pinsky and D. Avnir, *Inorg. Chem.,* 1998, **37**, 5575.

S11 D. Casanova, J. Cirera, M. Llunell, P. Alemany, D. Avnir and S. Alvarez, *J. Am. Chem. Soc.,* 2004, **126**, 1755.

S12 D. Casanova, M. Llunell, P. Alemany and S. Alvarez, *Chem. Eur. J.,* 2005, **11**, 1479.

S13 B. Sieklucka, R. Podgajny, P. Przychodzeń and T. Korzeniak, *Coord. Chem. Rev*., 2005, **249**, 2203.

S14 O. Kahn, *Molecular Magnetism*, VCH Publishers, New York, 1993.

S15 M. Liberka, M. Zychowicz, W. Zychowicz and S. Chorazy, *Chem. Commun*., 2022, **58**, 6381.

S16 D. Aravena and E. Ruiz, *Dalton Trans*., 2020, **49**, 9916.

S17 J. J. Zakrzewski, K. Kumar, M. Zychowicz, R. Jankowski, M. Wyczesany, B. Sieklucka, S. Ohkoshi and S. Chorazy, *J. Phys. Chem. Lett*., 2021, **12**, 10558.

S18 F. Neese, *WIREs Comput. Mol. Sci.*, 2018, **8**, e1327.

S19 F. Neese, *WIREs Comput. Mol. Sci.*, 2022, **12**, e1606.

S20 F. Neese, *WIREs Comput. Mol. Sci.*, 2025, **15**, e70019.

S21 F. Neese, F. Wennmohs, U. Becker and C. Riplinger, *J. Chem. Phys.*, 2020, **152**, 224108.

S22 F. Neese, *J. Comput. Chem.*, 2023, **44**, 381.

S23 Y. Zhao and D. G. Truhlar, *Theor. Chem. Acc.*, 2008, **120**, 215.

S24 F. Weigend and R. Ahlrichs, *Phys. Chem. Chem. Phys.*, 2005, **7**, 3297.

S25 E. Caldeweyher, C. Bannwarth and S. Grimme, *J. Chem. Phys.*, 2017, **147**, 034112.

S26 L. Wittmann, I. Gordiy, M. Friede, B. Helmich-Paris, S. Grimme, A. Hansen and M. Bursch, *Phys. Chem. Chem. Phys.*, 2024, **26**, 21379.

S27 E. Caldeweyher, J.-M. Mewes, S. Ehlert and S. Grimme, *Phys. Chem. Chem. Phys.*, 2020, **22**, 8499.

S28 E. Caldeweyher, S. Ehlert, A. Hansen, H. Neugebauer, S. Spicher, C. Bannwarth and S. Grimme, *J. Chem. Phys.*, 2019, **150**, 154122.

S29 F. Neese, *J. Comput. Chem.*, 2003, **24**, 1740.

S30 B. Helmich-Paris, B. de Souza, F. Neese and R. Izsák, *J. Chem. Phys.*, 2021, **155**, 104109.

S31 R. Izsák and F. Neese, *J. Chem. Phys.*, 2011, **135**, 144105.

S32 F. Neese, F. Wennmohs, A. Hansen and U. Becker, *Chem. Phys.*, 2009, **356**, 98.

S33 L. Blois, R. T. Moura Jr, R. L. Longo, O. L. Malta, H. F. Brito and A. N. Carneiro Neto, *J. Comput. Chem.*, 2025, **46**, e70034.

S34 I. Fdez. Galván, M. Vacher, A. Alavi, C. Angeli, F. Aquilante, J. Autschbach, J. J. Bao, S. I. Bokarev, N. A. Bogdanov, R. K. Carlson, L. F. Chibotaru, J. Creutzberg, N. Dattani, M. G. Delcey, S. S. Dong, A. Dreuw, L. Freitag, L. M. Frutos, L. Gagliardi, F. Gendron, A. Giussani, L. González, G. Grell, M. Guo, C. E. Hoyer, M. Johansson, S. Keller,

S. Knecht, G. Kovačević, E. Källman, G. Li Manni, M. Lundberg, Y. Ma, S. Mai, J. P. Malhado, P. Å. Malmqvist, P. Marquetand, S. A. Mewes, J. Norell, M. Olivucci, M. Oppel, Q. M. Phung, K. Pierloot, F. Plasser, M. Reiher, A. M. Sand, I. Schapiro, P. Sharma, C. J. Stein, L. K. Sørensen, D. G. Truhlar, M. Ugandi, L. Ungur, A. Valentini, S. Vancoillie, V. Veryazov, O. Weser, T. A. Wesołowski, P.-O. Widmark, S. Wouters, A. Zech, J. P. Zobel and R. Lindh, *J. Chem. Theory Comput.*, 2019, **15**, 5925.

S35 B. O. Roos, R. Lindh, P.-Å. Malmqvist, V. Veryazov and P.-O. Widmark, *J. Phys. Chem. A*, 2004, **108**, 2851.

S36 B. O. Roos, R. Lindh, P.-Å. Malmqvist, V. Veryazov and P.-O. Widmark, *J. Phys. Chem. A*, 2005, **109**, 6575.

S37 B. O. Roos, R. Lindh, P.-Å. Malmqvist, V. Veryazov, P.-O. Widmark and A. C. Borin, *J. Phys. Chem. A*, 2008, **112**, 11431.

S38 P. Å. Malmqvist, B. O. Roos and B. Schimmelpfennig, *Chem. Phys. Lett.*, 2002, **357**, 230.

S39 B. A. Heß, C. M. Marian, U. Wahlgren and O. Gropen, *Chem. Phys. Lett.*, 1996, **251**, 365.

S40 S. G. Duyker, G. J. Halder, P. D. Southon, D. J. Price, A. J. Edwards, V. K. Peterson and C. J. Kepert, *Chem. Sci.,* 2014*,* **5***,* 3409.

S41 R. E. Weston Jr and T. F. Brodasky, *J. Chem. Phys.*, 1957, **27**, 683.

S42 N.-N. Zhang, L.-D. Xin, L. Li, Y.-N. Zhang, P.-P. Wu, Y.-F. Han, Y. Yan and K.-G. Qu, *ACS Omega*, 2023, **8**, 34017.

S43 M. Niemiec, J. J. Zakrzewski, M. Reczyński and S. Chorazy, *Adv. Optical Mater.*, 2025, **13**, 2403564.